



1 **Multi-temporal high-resolution data products of ecosystem**  
2 **structure derived from country-wide airborne laser scanning**  
3 **surveys of the Netherlands**

4 Yifang Shi\* & W. Daniel Kissling

5 University of Amsterdam, Institute for Biodiversity and Ecosystem Dynamics (IBED), P.O. Box 94240,  
6 1090 GE Amsterdam, The Netherlands

7

8 *Correspondence to:* Yifang Shi ([y.shi@uva.nl](mailto:y.shi@uva.nl))

9

10

11 **Short summary**

12 We present a new set of multi-temporal LiDAR metrics of ecosystem structure derived from four  
13 national ALS surveys of the Netherlands (AHN1–AHN4), capturing vegetation height, cover, and  
14 structural variability over the past two decades (1998–2022). Around 70 TB point clouds have been  
15 processed to read-to-use raster layers at 10 m resolution (~ 59 GB), enabling a wide use and uptake of  
16 ecosystem structure information in biodiversity and habitat monitoring, ecosystem and carbon dynamic  
17 modelling.



## 18 **Abstract**

19 Recent years have seen a rapid surge in the use of Light Detection and Ranging (LiDAR) technology for  
20 characterizing the structure of ecosystems. Even though repeated airborne laser scanning (ALS) surveys  
21 are increasingly available across several European countries, only few studies have so far derived data  
22 products of ecosystem structure at a national scale, possibly due to a lack of free and open-source tools  
23 and the computational challenges involved in handling the large volumes of data. Nevertheless, high-  
24 resolution data products of ecosystem structure generated from multi-temporal country-wide ALS  
25 datasets are urgently needed if we are to integrate such information into biodiversity and ecosystem  
26 science. By employing a recently developed, open source, high-throughput workflow (named  
27 “Laserfarm”), we processed around 70 TB of raw point clouds collected from four national ALS surveys  
28 of the Netherlands (AHN1–AHN4, 1996–2022). This resulted in ~ 59 GB raster layers in GeoTIFF format  
29 as ready-to-use multi-temporal data products of ecosystem structure at a national extent. For each AHN  
30 dataset, we generated 25 LiDAR-derived vegetation metrics at 10 m spatial resolution, representing  
31 vegetation height, vegetation cover, and vegetation structural variability. The data enable an in-depth  
32 understanding of ecosystem structure at fine resolution across the Netherlands and provide opportunities  
33 for exploring ecosystem structural dynamics over time. To illustrate the utility of these data products, we  
34 present ecological use cases that monitor forest structural change and analyse vegetation structure  
35 differences across various Natura 2000 habitat types, including dunes, marshes, grasslands, shrublands,  
36 and woodlands. The provided data products and the employed workflow can facilitate a wide use and  
37 uptake of ecosystem structure information in biodiversity and carbon modelling, conservation science,  
38 and ecosystem management. The full data products are publicly available on Zenodo  
39 (<https://doi.org/10.5281/zenodo.13940846>) (Shi and Kissling 2024).

## 40 **1 Introduction**

41 Monitoring ecosystem structure is essential for sustainable forest management (Lindenmayer et al., 2000),  
42 species distribution research (Jetz et al., 2019; Kissling et al., 2018), dynamic ecosystem modelling  
43 (Kucharik et al., 2000), biodiversity monitoring (Noss, 1990), and the conservation and restoration of  
44 terrestrial ecosystems (Ruiz-Jaén and Aide, 2005). As one of the Essential Biodiversity Variables (EBVs)  
45 classes (Pereira et al., 2013), ecosystem structure provides detailed insights into both the vertical and  
46 horizontal profiles of ecosystems, facilitating a deeper understanding of the relationship between  
47 vegetation structure and animal ecology (Davies and Asner, 2014) as well as carbon and biomass  
48 dynamics (Zhao et al., 2018; Dalponte et al., 2019). However, until a decade ago, the collection of  
49 vegetation structure data was difficult and labour intensive, especially over large spatial scales (Davies  
50 and Asner, 2014). Although previous studies have explored the use of passive remote sensing  
51 technologies, such as high-resolution satellite imagery and aerial photographs, alongside field



52 measurements to obtain structural information (e.g. Wolter et al., 2009; Lamonaca et al., 2008), these  
53 applications have largely been confined to plot or local scales with limited scalability and uncertain  
54 transferability between different regions.

55 Over the past few decades, the advent of airborne laser scanning has enabled the direct  
56 measurement of ecosystem structural properties such as high-resolution topographic variation and  
57 accurate estimation of vegetation height, cover, and canopy structure (Lefsky et al., 2002). The LiDAR  
58 technology used in ALS surveys generates discrete returns (point clouds) and/or full-waveform signals  
59 by emitting laser pulses from the sensor towards the target objects (e.g. ground, trees, and buildings, etc),  
60 recording the distance between the sensor and the objects (“X”, “Y”, “Z” coordinates), the amount of  
61 energy returned to the sensor (“Intensity”), the type of the object (“Classification”), the sequence of  
62 returns generated from one pulse (“Return number” and “Number of returns”), the time of the pulse  
63 emitted (“GPS time”), and so on. Advances in sensor systems and techniques also allow many countries  
64 to carry out ALS campaigns over national or regional extents, producing fine-scale ecosystem  
65 measurements across broad spatial extents (Kissling et al., 2022; Assmann et al., 2022). ALS surveys  
66 often generate massive amounts of data (e.g. point clouds with a multi-terabyte data volume) which  
67 contain ecosystem structural information that is essential for ecological and biodiversity research  
68 (Kissling et al., 2022; Koma et al., 2021b; Bakx et al., 2019). Although tools and software for processing  
69 large amounts of LiDAR data are increasingly available (Roussel et al., 2020; Isenburg, 2017; Meijer et  
70 al., 2020; Kissling et al., 2022), significant challenges remain, including the need for specialist expertise,  
71 extensive data storage, and substantial computational power (Assmann et al., 2022). Ultimately,  
72 ecologists, foresters, biodiversity researchers and land managers require raster layers with structural  
73 information that can be readily integrated into analytical workflows using software that they are familiar  
74 with (e.g. GIS, R, Python). Such raster layers, e.g. LiDAR-derived vegetation metrics, are often generated  
75 by statistically aggregating the 3D point cloud information within spatial units such as voxels or 2D raster  
76 cells (Meijer et al., 2020; Kissling et al., 2022). These LiDAR-derived vegetation metrics typically capture  
77 three key dimensions of ecosystem structure: vegetation height (e.g. maximum vegetation height,  
78 vegetation height at a certain percentile), vegetation cover (e.g. the density of vegetation at a given height  
79 layer), and vegetation structural variability (e.g. the vertical or horizontal distribution and variability of  
80 vegetation within a spatial unit) (Kissling et al., 2023; Bakx et al., 2019). Providing high-resolution (~ 10  
81 m) ready-to-use LiDAR metrics and making them accessible for the public is, therefore, critical for  
82 monitoring Essential Biodiversity Variables (EBVs) (Valbuena et al., 2020), modelling species  
83 distributions (De Vries et al., 2021; Koma et al., 2021b; Zellweger et al., 2013), and estimating species  
84 diversity (Moeslund et al., 2019; Zellweger et al., 2017; Aguirre-Gutiérrez et al., 2017) at a regional or  
85 national scale.



86 Ecosystem structure is a three-dimensional phenomenon with horizontal and vertical components  
87 that change over time (Zenner and Hibbs, 2000). The increasing frequency of ALS data acquisition offers  
88 a unique opportunity to monitor ecological changes and ecosystem dynamics at fine spatial and temporal  
89 scales. Several countries have been conducting repeated (sub-)national ALS surveys to obtain fine-scale  
90 information on topography and forest ecosystems (Nilsson et al., 2017). For example, the Dutch national  
91 ALS programme (AHN, *Actueel Hoogtebestand Nederland*, <https://www.ahn.nl/>) has been collecting  
92 country-wide LiDAR data since 1996, providing four complete ALS datasets (AHN1–AHN4) with an  
93 ongoing fifth survey (AHN5), conducted at intervals of 3 to 5 years. In Spain, under the PNOA-LiDAR  
94 project, two national ALS campaigns have taken place during 2008–2015 (LiDAR 1<sup>st</sup> coverage) and  
95 during 2015–2021 (LiDAR 2<sup>nd</sup> coverage), while the third acquisition (LiDAR 3<sup>rd</sup> coverage) has started in  
96 2023 and is planned to finish in 2025  
97 (<http://centrodedescargas.cnig.es/CentroDescargas/catalogo.do?Serie=LIDAR>, last access: 19 October  
98 2024). While the primary goal of many ALS campaigns is to produce terrain models, such as Digital  
99 Terrain Models (DTMs) or Digital Surface Models (DSMs), the multi-temporal LiDAR datasets also  
100 capture detailed 3D characteristics on vegetation structure over time, providing valuable information for  
101 evaluating changes in biomass (Cao et al., 2016; Feng et al., 2024), forest structure (Mccarley et al., 2017;  
102 Riofrío et al., 2022; Vepakomma et al., 2011), and forest carbon stocks (Dalponte et al., 2019; Zhao et  
103 al., 2018). Furthermore, these datasets are increasingly being integrated with other remote sensing data,  
104 such as satellite imageries from Landsat, Sentinel-2, and synthetic aperture radar (SAR), to assess forest  
105 changes caused by disturbances like wildfires (Li et al., 2023; Feng et al., 2024) and to model  
106 aboveground biomass (Musthafa and Singh, 2022). However, despite the growing availability of multi-  
107 temporal ALS datasets, there is a noticeable lack of publicly available data products, i.e. LiDAR-derived  
108 vegetation metrics, from national ALS surveys.

109 Several challenges are posed in generating accurate and standardized data products from multi-  
110 temporal ALS data (Valbuena et al., 2020). Over the past three decades, advances in LiDAR sensors and  
111 associated technologies have led to improvements in point density, classification accuracy, and additional  
112 attributes provided in each point (Riofrío et al., 2022). However, these advancements also introduce  
113 complexities in data harmonization. In addition to the challenges associated with processing large datasets  
114 and high computational costs (Meijer et al., 2020), discrepancies in sensor technology and flight  
115 configurations across different ALS surveys can hinder the generation of consistent data products (Lin et  
116 al., 2022). For instance, the first Dutch national ALS campaign (AHN1, 1996–2003) had an average point  
117 density ranging from 1 point per 16 square meters to 1 point per square meter, with no detailed point  
118 classification available. By contrast, in the fourth campaign (AHN4, 2020–2022), the point density has  
119 improved to 20–30 points per square meter, with detailed classification code provided for each point  
120 following the ASPRS standard (Asprs, 2019). These technological variations inevitably result in data  
121 products with varying quality and accuracy, introducing uncertainties in their usability (Tompalski et al.,





122 2021; Hopkinson et al., 2008). To understand ecosystem dynamics accurately, changes detected from  
123 multi-temporal ALS datasets should reflect actual ecological changes in the target of interest rather than  
124 differences in data acquisition or quality (Riofrío et al., 2022). Identifying the limitations and providing  
125 usage notes of derived data products are important for users to interpret the data products correctly and  
126 apply them optimally in their analyses.

127 Here, we present a new set of multi-temporal data products of ecosystem structure derived from  
128 four national ALS surveys of the Netherlands (AHN1–AHN4). The data products, with a spatial  
129 resolution of 10 m, include four sets of 25 LiDAR-derived vegetation metrics representing ecosystem  
130 height, vegetation cover, and structural variability, aimed at supporting a wide range of ecological  
131 applications. In this paper, we (1) describe the ALS data collection from AHN1–AHN4 and the employed  
132 “Laserfarm” workflow to generate the data products, (2) present the detailed characteristics of the  
133 generated multi-temporal data products (i.e. LiDAR-derived vegetation metrics as GeoTIFF raster layers)  
134 and their known limitations and corresponding usage notes, (3) demonstrate two use cases for using the  
135 generated data products in ecological applications, and (4) discuss the potential use and recommendations  
136 for utilizing these data products in future research. To facilitate open science, we make the data products,  
137 employed workflow, Python script, and related documentation publicly available. We anticipate that this  
138 will not only allow the upscaling of ecological and biodiversity research but also benefit a broad range of  
139 scientists and decision-makers who are interested in using ecosystem structure information for  
140 environmental monitoring and management.

## 141 **2 Raw data and processing workflow**

### 142 **2.1 Geography and ecology of the Netherlands**

143 The Netherlands is situated in Northwest Europe (52°22'N, 4°53'E), covering a total land area of 33893  
144 km<sup>2</sup>. It has mostly flat coastal lowlands and reclaimed land (polders) with an average elevation of  
145 approximately 30 meters above sea level. The primary ecosystems in the Netherlands include agricultural  
146 land, dunes and beaches, forests, wetlands, grasslands, and other (semi)natural environments (Hein et al.,  
147 2020). The Netherlands has a temperate maritime climate with continental influence, resulting in an  
148 average annual precipitation of 854.7 mm and a mean temperature of 10.5 °C.

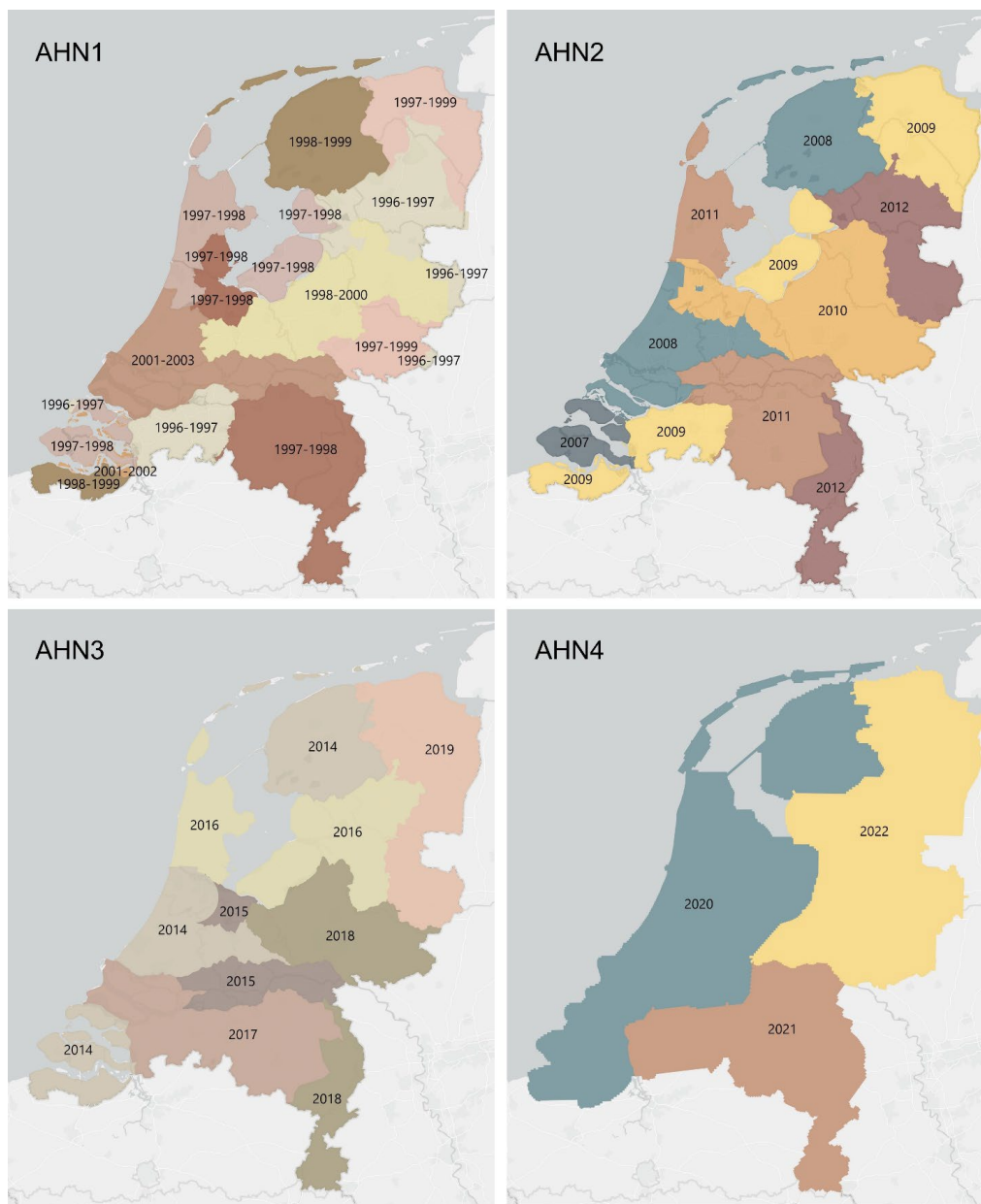
### 149 **2.2 Four Dutch national ALS campaigns**

150 The initial purpose of the AHN programme was to monitor and manage water systems in the Netherlands.  
151 It is a collaboration between 26 regional water boards, provinces and Rijkswaterstaat (the executive  
152 directorate general for public works and water management of the Dutch government) with the aim of  
153 producing accurate digital elevation models of the Netherlands. To minimize the impact of foliage on  
154 ground detection during the laser scanning, the AHN data acquisition is performed in the winter period,



155 from December to April. The first generation of AHN (AHN1) was conducted during 1996–2003, with a  
156 point density of 1 point per 1–16 square meters, which largely depended on the viability of the technology  
157 and the date of acquisition (Swart, 2010). Due to errors in the AHN1 data (e.g. inaccuracies in the inertial  
158 navigation system, misalignment of overlapping scanning strips, and the presence of artifacts), the data  
159 quality of AHN1 is rather poor, especially for areas covered by vegetation (Brand et al., 2003). To support  
160 both water and dike management, the second generation of AHN (AHN2) was started in 2007, with  
161 improved specifications such as a higher point density (on average 6–10 pts m<sup>-2</sup>) and a higher  
162 planimetric/vertical accuracy (5–15 cm). It also required some raster data (i.e. DTMs and DSMs) to be  
163 delivered with grid cell sizes of 0.5 m and 5 m. With the main aim of obtaining terrain surface information,  
164 both AHN1 and AHN2 datasets were delivered in two separate parts: point clouds representing the terrain  
165 (“gefilterde puntenwolk”) and point clouds representing non-ground points, i.e. trees, buildings, bridges  
166 and other objects (“uitgefilterde puntenwolk”).

167 Benefitting from the advances in LiDAR sensors and related technologies, the third generation of  
168 AHN (AHN3) provided not only a higher density of point clouds, but also more information stored for  
169 each point, such as point classification code, intensity values, number of returns, and so on (Table 1).  
170 Even though both AHN2 and AHN3 were collected within a 6-year cycle (2007–2012 for AHN2, and  
171 2014–2019 for AHN3), the actual time difference between AHN2 and AHN3 varies between 4–10 years  
172 depending on the area of interest (Fig. 1). For the latest completed AHN (AHN4), the survey was  
173 conducted between 2020 and 2022 (3-year cycle), making the country-wide dataset more quickly  
174 available for the whole Netherlands. All four AHN datasets were provided in LAZ format (i.e. version  
175 1.2 for AHN1–AHN3, and version 1.4 for AHN4), under the local Dutch coordinate system “RD\_new”  
176 (EPSG: 28992, NAP:5709). The datasets from AHN1 to AHN4 show an increase in data volume and  
177 improved classification as well as additional attributes stored for each point (Table 1). An ongoing fifth  
178 ALS survey (AHN5) has started in 2023 (the first part of the data is available, see  
179 <https://www.ahn.nl/heel-westelijk-nederland-gereed>) and the data acquisition will be completed in 2025.



180

181 Fig.1 Data acquisition times for AHN1–AHN4. Different colours indicate the different years of data  
 182 collection for each dataset.

183

184 **Table 1.** Summary of raw point cloud characteristics collected by different AHN surveys (AHN1–  
 185 AHN4). Some flight configurations are not available, for instance, the type of sensor, the flight height,  
 186 flight speed, and the scan angle, especially for the AHN1 dataset. NAP: Normal Amsterdam Level.

Data characteristic	AHN1	AHN2	AHN3	AHN4
Acquisition year	1996–2003	2007–2012	2014–2019	2020–2022



Acquisition season	Leaf-off	Leaf-off	Leaf-off	Leaf-off
Horizontal projection	RD_new	RD_new	RD_new	RD_new
Vertical projection	NAP	NAP	NAP	NAP
Point density (pts m <sup>-2</sup> )	0.05–1	6–15	10–20	20–30
Scan angle (°)	-	± 30	± 35	± 35
Overlapping rate	-	20–35%	20–35%	20–35%
Point cloud format	Laz (1.2)	Laz (1.2)	Laz (1.2)	Laz (1.4)
Vertical accuracy (cm)	5–35	5–15	5–15	5–10
Number of files	2720	60185	1367	1381
Data volume (compressed)	33.1 GB	986.7 GB	2564.8 GB	6408.6GB
Attributes in each point	X, Y, Z	X, Y, Z	X, Y, Z, intensity, return number, number of returns, classification, scan angle, point ID, GPS time	X, Y, Z, intensity, return number, number of returns, classification, scan angle, point ID, GPS time, amplitude, reflectance, deviation
Classification	uitgefilterd (0) gefilterd (0)	uitgefilterd (0) gefilterd (0)	unclassified (1) ground (2) building (6) water (9) reserved (26)	unclassified (1) ground (2) building (6) water (9) powerline (14) reserved (26)
Available additional layers	-	DSM, DTM	DSM, DTM	DSM, DTM

187

### 188 2.3 Processing workflow

189 We employed the high-throughput workflow “Laserfarm” (<https://laserfarm.readthedocs.io/en/latest/>) to  
 190 process the multi-temporal AHN datasets. Laserfarm is an open-source workflow designed for processing  
 191 large amount of LiDAR point cloud data into geospatial data products of ecosystem structure (Kissling et  
 192 al., 2022). It consists of four main modules: (1) re-tiling, where the original LAZ files (covering 5 km ×  
 193 6.5 km per tile) are re-tiled into 1 km × 1 km LAZ files for an efficient, scalable and distributed processing;  
 194 (2) normalization, where the height (z value) of the lowest point within a 1 m × 1 m grid cell is subtracted  
 195 from each point in the cell, so that the influence of terrain on the height of above-ground points is removed  
 196 from subsequent processing; (3) feature extraction, where user-defined features (e.g. LiDAR metrics such  
 197 as the 95<sup>th</sup> percentile of vegetation height and the skewness of vegetation height) are calculated at 10

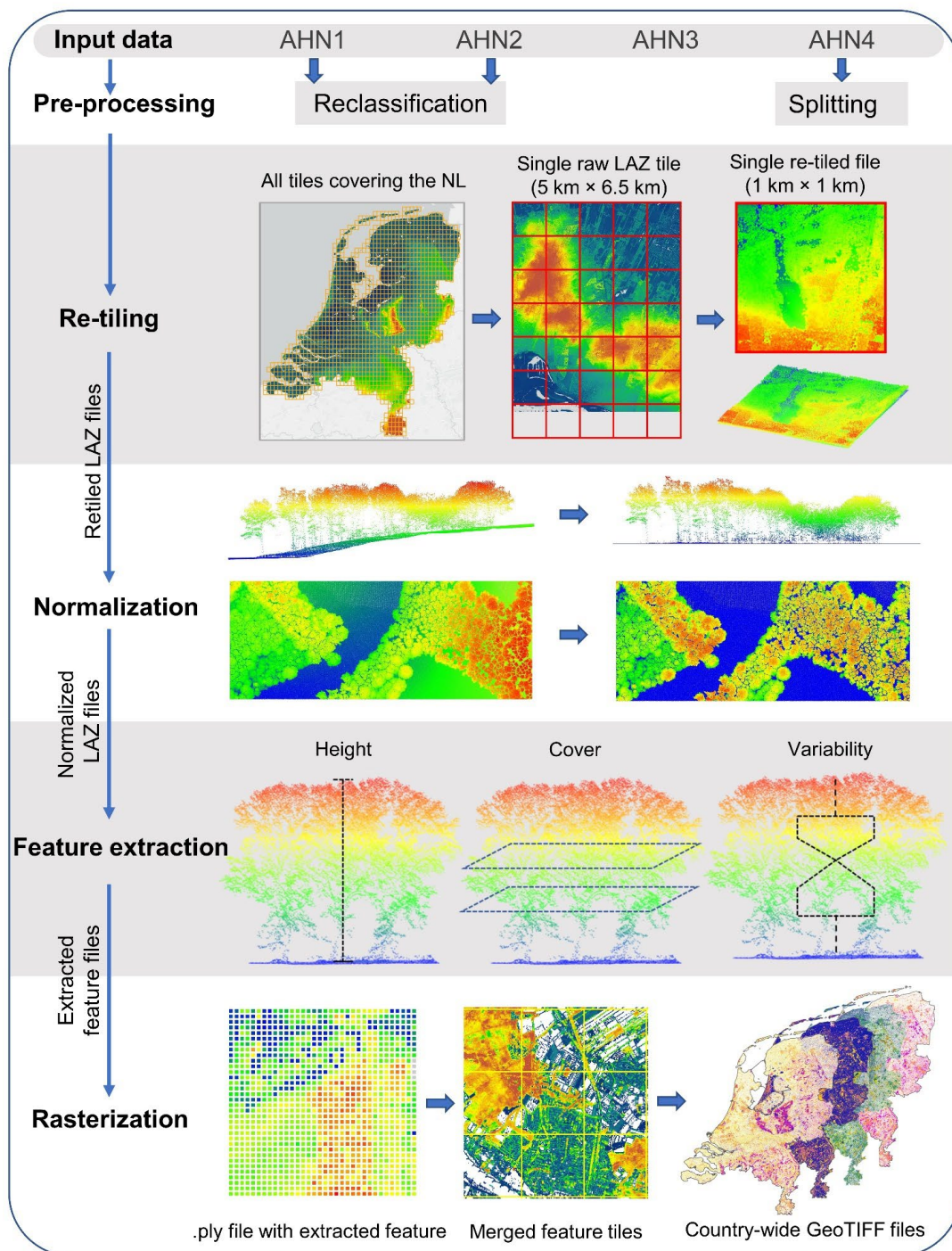


198 meter resolution using points within an infinite square cell (Meijer et al., 2020); and (4) rasterization,  
199 where the extracted feature files (.PLY files) are merged and exported as single-band GeoTIFF raster  
200 files. Note that in all four AHN datasets, vegetation points are not classified separately based on the  
201 ASPRS standard. Instead, they are assigned a classification value 0 (“uitgefilterd”) in AHN1 and AHN2,  
202 and a value 1 (“unclassified”) in AHN3 and AHN4. These classification values were used as vegetation  
203 class during the feature extraction. We chose the Laserfarm workflow to process the four country-wide  
204 AHN datasets because (1) it enables the efficient, scalable and distributed processing of multi-terabyte  
205 LiDAR point clouds at a national scale, (2) it is a free and open-source tool implemented in Python and  
206 available as Jupyter Notebooks, and (3) it allows the automated generation of consistent and reproducible  
207 geospatial data products of ecosystems structure from different ALS data.

208 Due to the different characteristics of each AHN dataset (Table 1), several pre-processing steps  
209 were implemented before executing the main modules of the Laserfarm workflow (Fig. 2). In particular,  
210 for the AHN1 and AHN2 datasets, the step “Reclassification” was carried out before re-tiling, as both  
211 datasets only have “gefilterd” (ground) and “uitgefilterd” (non-ground) files provided and the raw  
212 classification value was set to 0 (never classified) for all points. We therefore reassigned a classification  
213 value “2” to the ground points (“gefilterd”) and a classification value “0” to the non-ground points  
214 (“uitgefilterd”). These classification values were later used for the normalization and feature extraction.  
215 For the AHN4 dataset, the volume of a single original LAZ file varies from 0.3 MB to 16.5 GB, with an  
216 average size of 4.6 GB per file (Table 2). Since handling such volumes is challenging for many computing  
217 infrastructures (due to their CPUs and random-access memory, RAM), we applied a “Splitting” step  
218 before the re-tiling (Fig. 2), with a maximum data volume of ~ 500 MB being used for splitting the original  
219 tiles into smaller ones.

220





221  
222 Fig. 2 Overview of the processing workflow employed for four country-wide AHN datasets of the  
223 Netherlands (AHN1–AHN4). The pre-processing step “reclassification” was only conducted for the  
224 AHN1 and AHN2 datasets, where ground points were reassigned a classification value “2”. The  
225 “splitting” step was added to split the large LAZ files from AHN4 into smaller ones before re-tiling. Re-  
226 tiling, normalization, feature extraction and rasterization are four main modules of the Laserfarm



227 workflow, which have been applied for all four AHN datasets to generate country-wide LiDAR-derived  
228 vegetation metrics. The input data were raw LAZ files with different point density, and the output data  
229 were 25 single-band GeoTIFF raster layers at 10 meter resolution for each AHN dataset.

## 230 **2.4 IT infrastructure and computational cost**

231 All four AHN datasets were processed on the IT infrastructure services provide by SURF, the Dutch  
232 national facility for information and communication technology (<https://www.surf.nl/>). Specifically, we  
233 used the dCache platform for data storage (<https://www.surf.nl/en/services/dcache>) and the HPC Cloud  
234 (<https://www.surf.nl/en/services/hpc-cloud>) or Spider platform ([https://www.surf.nl/en/services/high-  
235 performance-data-processing](https://www.surf.nl/en/services/high-performance-data-processing)) for high-performance data processing. The data processing platforms have  
236 fast access to the data storage while enabling scalable and flexible processing of multi-terabytes datasets  
237 on distributed resources. We first downloaded the raw AHN1–AHN4 LiDAR point clouds from the  
238 PDOK webservices (<https://www.pdok.nl/introductie/-/article/actueel-hoogtebestand-nederland-ahn>) to  
239 the dCache data storage using a customized python script  
240 ([https://github.com/ShiYifang/AHN/tree/main/AHN\\_downloading](https://github.com/ShiYifang/AHN/tree/main/AHN_downloading)). We then ran the Laserfarm  
241 workflow for processing the AHN1–AHN3 datasets on the HPC Cloud, where we set up a cluster of 11  
242 VMs, each VM with 2 cores, 32 GB or 64 GB RAM, and 256 GB local HDD. Due to migration of the  
243 computing resources by SURF (from HPC Cloud to Spider), we processed the AHN4 dataset with the  
244 Laserfarm workflow on Spider, where a number of flexible and customisable workers with assigned CPU  
245 cores were defined based on the computing requirement for each workflow step. We used 2–10 workers,  
246 each with 2–4 cores and 16–32 GB RAM for splitting, re-tiling, normalization, and feature extraction,  
247 and 2 workers, each with 12 cores and 94 GB RAM for the rasterization step. All input data (i.e. raw LAZ  
248 files), intermediate results (e.g. re-tiled LAZ files, normalized LAZ files, featured PLY tiles), and final  
249 output (i.e. GeoTIFF raster layers) were automatically stored (and/or retrieved for the next step) on the  
250 dCache data storage.

251 The computing time for each AHN dataset varies based on the input data volume, the required  
252 processing steps (Table 2), and the settings of the employed infrastructure. The increase in data volumes  
253 from AHN1 to AHN4 resulted in a strong increase of the processing time (Table 2). In total, it required  
254 57.6 days (wall-time) to process the multi-temporal AHN datasets (AHN1–AHN4). The AHN1 (data  
255 volume of 33.1 GB) only took a wall-time of 4.8 days to complete whereas the AHN4 (data volume of  
256 6408.6 GB) took a total wall-time of 26.8 days. It is worth noting that the actual computing time of the  
257 process might be longer than the wall-time estimates, e.g. due to processing errors, worker failures, and  
258 system maintenance.

259

260

261



262 **Table 2.** Overview of the number of input files, the total volume and the average volume per file for each  
 263 processing step, and the total processing wall-time for each AHN dataset. Note that the total wall-time  
 264 was estimated based on different infrastructure settings for processing the AHN1–AHN3 (HPC Cloud)  
 265 and AHN4 (Spider) datasets.

Data characteristic	AHN1	AHN2	AHN3	AHN4
<i>Input for re-tiling</i>	<i>(Reclassified)</i>	<i>(Reclassified)</i>		<i>(Splitted)</i>
Number of input files	2720	60185	1367	18797
Total volume	33.1 GB	986.7 GB	2564.8 GB	6408.6 GB
Average volume per file (mean ± SD)	12.20 ± 10.68 MB	16.40 ± 14.73 MB	1.75 ± 0.93 GB	4.60 ± 2.41 GB
<i>Re-tiling</i>				
Number of re-tiled files	37715	37627	37457	37990
Total volume	33.1 GB	986.7 GB	2564.8 GB	6408.6 GB
Average volume per file (mean ± SD)	0.83 ± 1.64 MB	26.90 ± 35.98 MB	0.07 ± 0.18 GB	0.17 ± 0.09 GB
<i>Normalization</i>				
Number of normalized files	37715	37627	37457	37990
Total volume	64.0 GB	3682.4 GB	6067.5 GB	9593.3 GB
Average volume per file (mean ± SD)	1.70 ± 2.13 MB	97.87 ± 59.23 MB	0.16 ± 0.09 GB	0.25 ± 0.13 GB
<i>Feature extraction</i>				
Number of featured files	37715 × 25	37627 × 25	37457 × 25	37990 × 25
Total volume	257.1 GB	282.5 GB	285.9 GB	212.5 GB
Average volume per file (mean ± SD)	0.29 ± 0.02 MB	0.30 ± 0.03 MB	0.33 ± 0.05 MB	0.23 ± 0.04 MB
<i>Rasterization</i>				
Number of rasterized files	25	25	25	25
Total volume	4.8 GB	19.4 GB	18.8 GB	15.6 GB
Average volume per file (mean ± SD)	202.1 ± 101.6 MB	774.5 ± 303.5 MB	759.8 ± 226.2 MB	625.5 ± 160.7 MB
<i>Processing time</i>				
Total processing wall-time (days)	4.8	11.7	14.3	26.8





## 267 **3 Data products description**

### 268 **3.1 Overview of data products**

269 The generated data products from each AHN campaign cover the whole Netherlands, ranging from 50.77  
270 °N to 53.36 °N and from 3.57 °E to 7.11 °E. The data products are provided as 10 meter resolution  
271 GeoTIFF raster files (25 single-band raster layers for each AHN dataset) in the local Dutch coordinate  
272 system “RD\_new” (EPSG: 28992, NAP:5709). The total volume of the four data products is  
273 approximately 58.6 GB. The pixel value is stored in 32 bit floating point precision. The data products are  
274 freely accessible via a permanent Zenodo repository (see Sect. 7).

### 275 **3.2 LiDAR-derived vegetation metrics**

276 In total, 25 LiDAR-derived vegetation metrics were generated from each AHN dataset, representing  
277 vegetation height, vegetation cover, and vegetation structure variability (Table 3). For vegetation height,  
278 we generated 7 LiDAR metrics (i.e. maximum, mean, median, 25<sup>th</sup>, 50<sup>th</sup>, 75<sup>th</sup>, 95<sup>th</sup> percentile of vegetation  
279 height) representing the height of vegetation at the canopy surface and for low, middle, and upper  
280 vegetation strata (Fig. 3a). We filtered out the points with a z value higher than 10000 m (outliers) during  
281 “Normalization” step of the Laserfarm workflow and used a square infinite cell (10 × 10 m) as the target  
282 volume to calculate the height metrics (see detailed description of target volumes in Meijer et al. (2020)).  
283 To ensure positive height values after normalization, we generally normalized the vegetation points based  
284 on the height of the lowest point within a 1 m × 1 m grid cell. For vegetation cover, we derived 11 LiDAR  
285 metrics consisting of one metric describing the openness of vegetation (i.e. pulse penetration ratio), one  
286 metric describing the density of upper vegetation layer (i.e. canopy cover), and 9 metrics quantifying  
287 vegetation density at different height layers (i.e. below 1 m, between 1–2 m, 2–3 m, 3–4 m, 4–5 m, 5–20  
288 m, above 3 m, below 5 m, and above 20 m) (Fig. 3b). The height layers reflect the most relevant height  
289 strata to capture the vegetation distribution of major growth forms (e.g. grass, reed, shrubs and trees)  
290 (Morsdorf et al., 2010; Miura and Jones, 2010). Special attention was given to represent low vegetation  
291 strata (1–5 m) as they are essential for low-stature terrestrial ecosystems such as grasslands, shrublands  
292 or agricultural areas when monitoring animal habitats and species distributions (Koma et al., 2021a; Bakx  
293 et al., 2019). Note that the pulse penetration ratio is the only LiDAR metric (among the 25 metrics) that  
294 used ground points for the calculation. All other 24 metrics are only calculated with vegetation points (i.e.  
295 “unclassified” in AHN). For vegetation structural variability, we derived 7 LiDAR metrics representing  
296 the vertical variability of vegetation distribution within a cell (Fig. 3c), including the coefficient of  
297 variation, Shannon index, kurtosis, skewness, standard deviation, variance, and roughness (sigma) of  
298 vegetation height. The detailed description of how those metrics are calculated and their ecological  
299 relevance can be found in Table 3.

300



301 **Table 3.** Twenty-five LiDAR-derived vegetation metrics capturing ecosystem structure in three key  
 302 dimensions (vegetation height, vegetation cover and vegetation structural variability), together with their  
 303 file names in the data products, the formulas for calculation, their descriptions and example of their  
 304 ecological relevance. Each LiDAR metric is provided as a single-band GeoTIFF raster layer at 10 meter  
 305 resolution, with the file name “ahn#\_10m\_xx”, where # is the number of AHN campaign (“1–4”) and xx  
 306 is the name of the LiDAR metrics. For instance, “ahn4\_10m\_perc\_95\_normalized\_height” represents the  
 307 95<sup>th</sup> percentile of vegetation height derived from the AHN4 dataset. For the calculation formulas,  $N$  is the  
 308 total number of normalized vegetation points within a cell,  $z_i$  represents all normalized  $z$  values in a cell,  
 309 and  $\bar{z}$  is the mean normalized  $z$  value in a cell.  
 310

LiDAR metric (abbreviation)	File name (ahn#_10m_xx)	Calculation formula	Description	Ecological relevance
<i>Vegetation height</i>				
Maximum vegetation height (Hmax)	max_normalized_height	$z_{max}$	Maximum of normalized $z$ within a cell	Height of canopy surface, tree tops
Mean of vegetation height (Hmean)	mean_normalized_height	$z_{mean}$	Mean of normalized $z$ within a cell	Average height of vegetation, mean tree height
Median of vegetation height (Hmedian)	median_normalized_height	$z_{median}$	Median of normalized $z$ within a cell	Vegetation height, vertical distribution of vegetation
25th percentiles of vegetation height (Hp25)	perc_25_normalized_height	$z_{25\ percentile}$	25 <sup>th</sup> percentile of normalized $z$ within a cell	Density of vegetation in the low stratum
50th percentiles of vegetation height (Hp50)	perc_50_normalized_height	$z_{50\ percentile}$	50 <sup>th</sup> percentile of normalized $z$ within a cell. It corresponds to the Hmedian.	Average height and vertical distribution of vegetation
75th percentiles of vegetation height (Hp75)	perc_75_normalized_height	$z_{75\ percentile}$	75 <sup>th</sup> percentile of normalized $z$ within a cell	Density of vegetation in the upper stratum
95th percentiles of vegetation height (Hp95)	perc_95_normalized_height	$z_{95\ percentile}$	95 <sup>th</sup> percentile of normalized $z$ within a cell	Height of the vegetation canopy surface, avoiding the effect of outliers (compared to Hmax)
<i>Vegetation cover</i>				



Pulse penetration ratio (PPR)	pulse_penetration_ratio	$\frac{N_{ground}}{N_{total}}$	Ratio of number of ground points to total number of points within a cell	Openness of vegetation, canopy fractional cover, laser penetration index
Canopy cover (Density_above_mean_z)	density_absolute_mean_normalized_height	$100 \times \sum [z_i > \bar{z}]/N$	Number of returns above mean height within a cell	Density of upper vegetation layer
Density of vegetation points below 1 m (BR_below_1)	band_ratio_normalized_height_1	$N_{z<1}/N_{total}$	Ratio of number of vegetation points below 1 m to the total number of vegetation points within a cell	Density of vegetation below 1 m
Density of vegetation points between 1–2 m (BR_1_2)	band_ratio_1_normalized_height_2	$N_{1<z<2}/N_{total}$	Ratio of number of vegetation points between 1–2 m to the total number of vegetation points within a cell	Density of vegetation in 1–2 m layer
Density of vegetation points between 2–3 m (BR_2_3)	band_ratio_2_normalized_height_3	$N_{2<z<3}/N_{total}$	Ratio of number of vegetation points between 2–3 m to the total number of vegetation points within a cell	Density of vegetation in 2–3 m layer
Density of vegetation points above 3 m (BR_above_3)	band_ratio_3_normalized_height	$N_{z>3}/N_{total}$	Ratio of number of vegetation points above 3 m to the total number of vegetation points within a cell	Density of vegetation in above 3 m layer
Density of vegetation points between 3–4 m (BR_3_4)	band_ratio_3_normalized_height_4	$N_{3<z<4}/N_{total}$	Ratio of number of vegetation points between 3–4 m to the total number of vegetation points within a cell	Density of vegetation in 3–4 m layer
Density of vegetation points between 4–5 m	band_ratio_4_normalized_height_5	$N_{4<z<5}/N_{total}$	Ratio of number of vegetation points between 4–5 m to the total number of	Density of vegetation in 4–5 m layer

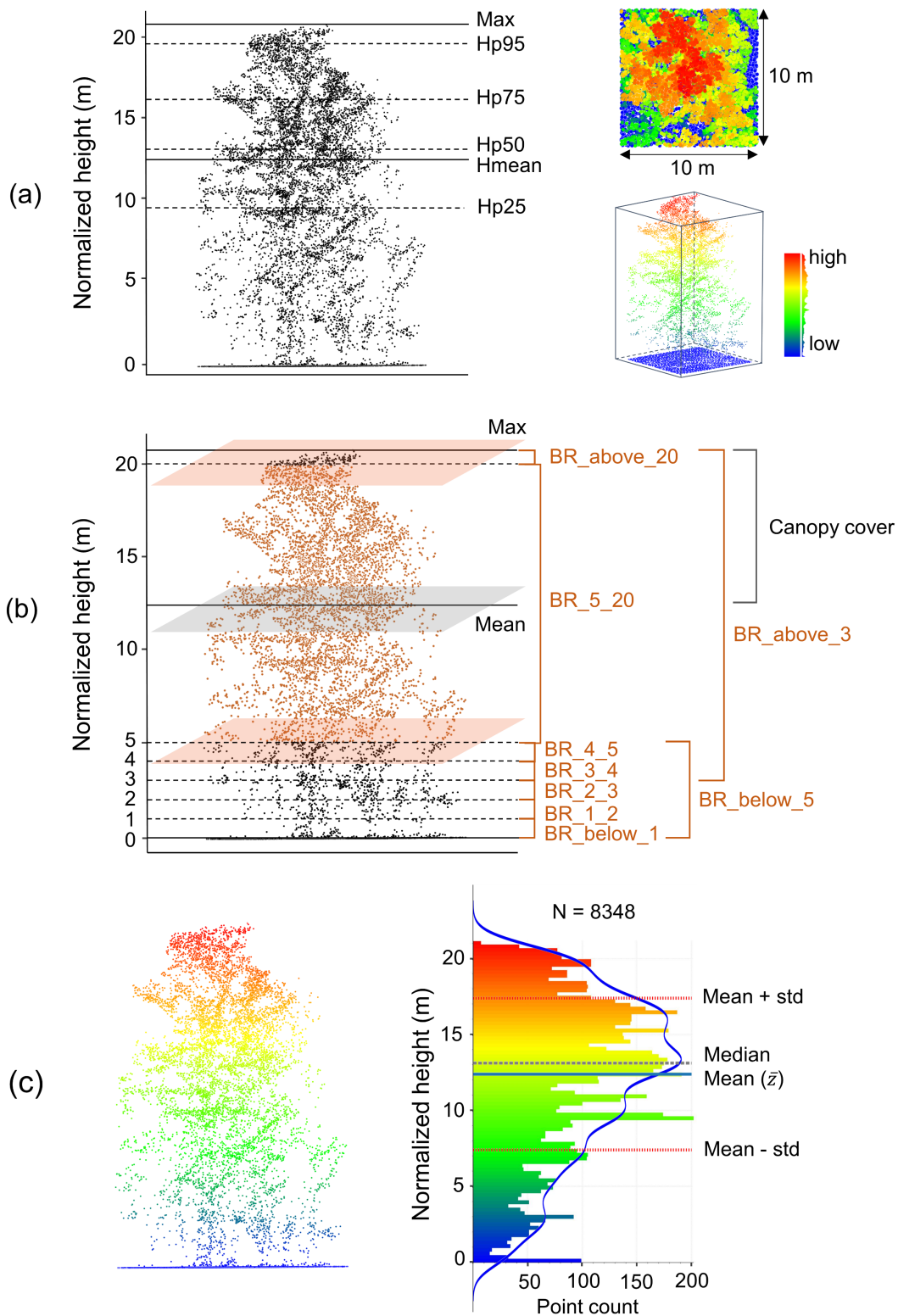


4–5 m (BR_4_5)			vegetation points within a cell	
Density of vegetation points below 5 m (BR_below_5)	band_ratio_norm alized _height_5	$N_{z<5}/N_{total}$	Ratio of number of vegetation points below 5 m to the total number of vegetation points within a cell	Density of vegetation below 5 m
Density of vegetation points between 5–20 m (BR_5_20)	band_ratio_5_nor malized_ height_20	$N_{5<z<20}/N_{total}$	Ratio of number of vegetation points between 5–20 m to the total number of vegetation points within a cell	Density of vegetation in 5–20 m layer
Density of vegetation points above 20 m (BR_above_20)	band_ratio_20_n ormalized_ height	$N_{z>20}/N_{total}$	Ratio of number of vegetation points above 20 m to the total number of vegetation points within a cell	Density of vegetation in above 20 m layer
<i>Vegetation structural variability</i>				
Coefficient of variation of vegetation height (Coeff_var)	coeff_var_ normalized_heig ht	$\frac{1}{\bar{z}} \times \sqrt{\sum \frac{(z_i - \bar{z})^2}{N - 1}}$	Coefficient of variation of normalized z within a cell	Vertical variability of vegetation distribution
Shannon index (Entropy_z)	entropy_ normalized_heig ht	$-\sum_i p_i \times \log_2 p_i$ where $p_i = N_i / \sum_j N_j$ , and $N_i$ is the points in bin $i$ .	The negative sum of the proportion of points within 0.5 m height layers multiplied with the logarithm of the proportion of points within 0.5 m height layers within a cell	Vertical complexity of vegetation, foliage height diversity
Kurtosis of vegetation height (Hkurt)	kurto_ normalized_heig ht	$\frac{1}{\sigma^4} \times \sum (z_i - \bar{z})^4 / N$ where $\sigma$ is the standard deviation of the z value in a cell.	Kurtosis of normalized z within a cell	Vertical distribution of vegetation



Roughness of vegetation (Sigma_z)	sigma_z	$\sqrt{\sum(R_i - \bar{R})^2 / (N - 1)}$ where $R_i$ are the residual after plane fitting, and $\bar{R}$ the mean of residuals.	Standard deviation of the residuals of a locally fitted plane within a cylinder	Small-scale roughness and variability of vegetation
Skewness of vegetation height (Hskew)	skew_normalized_heig ht	$\frac{1}{\sigma^3} \times \sum (z_i - \bar{z})^3 / N$	Skewness of normalized z within a cell	Vertical distribution of vegetation
Standard deviation of vegetation height (Hstd)	std_normalized_heig ht	$\sqrt{\sum \frac{(z_i - \bar{z})^2}{N - 1}}$	Standard deviation of normalized z within a cell	Vertical variability of vegetation distribution
Variance of vegetation height (Hvar)	var_normalized_heig ht	$\sum \frac{(z_i - \bar{z})^2}{N - 1}$	Variance of normalized z within a cell	Vertical variability of vegetation distribution

311  
 312



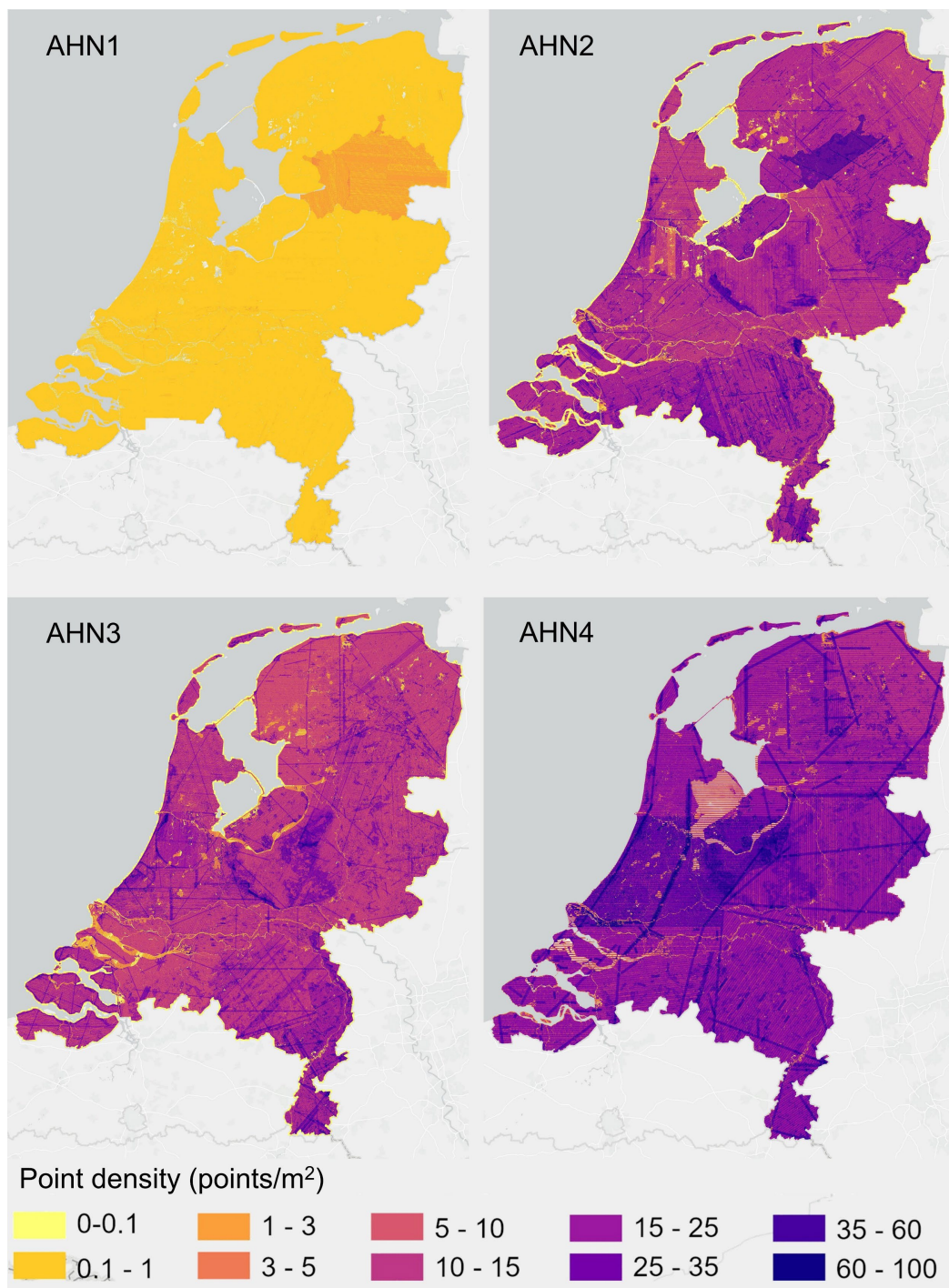


314 Fig 3. Examples of LiDAR metric generation in a  $10\text{ m} \times 10\text{ m}$  grid cell (the number of all points:  $N =$   
315 8348). (a) Metrics of vegetation height (mean, max, and percentiles of normalized height). (b) Vegetation  
316 cover metrics representing vegetation density within specific height layers. (c) Metrics of vegetation  
317 structural variability (e.g. standard deviation and variance of vegetation height are calculated based on  
318 mean height  $\bar{z}$ ; kurtosis and skewness of vegetation height are calculated based on the standard deviation  
319 and mean height within a cell) (see detailed calculation formula in Table 3). The blue line in (c) represents  
320 a kernel density estimate (KDE) showing the shape of the points distribution. See abbreviation and  
321 calculation formula of all metrics in Table 3.

### 322 3.3 Auxiliary data

323 Since the point density of AHN datasets changes across space and time, we also provide a raster layer of  
324 point density (using all point classes) for each AHN dataset (four in total) (Fig. 4). The AHN1 has a much  
325 lower point density (average less than  $0.5\text{ pts m}^{-2}$ ) throughout the whole country than other AHN datasets  
326 due to sensor limitations back in 1996. AHN2 and AHN3 have a similar point density (on average  $10\text{--}20$   
327  $\text{pts m}^{-2}$ ), while AHN4 has the highest point density ( $25\text{--}30\text{ pts m}^{-2}$ ). Especially for the AHN2–AHN4  
328 datasets, distinct patterns (patches, lines, edges) can be observed in different parts of the Netherlands.  
329 They are partially due to the influence of the water surface (yellow areas in AHN2, AHN3, and AHN4,  
330 Fig. 4), but also related to flight lines and operational configurations (e.g. flying altitude and flight speed)  
331 during the campaign.





332

333 Fig. 4 Point density of AHN1–AHN4 ALS campaigns across the Netherlands. The total number of points  
334 was used for calculating the density of points at 10 meter spatial resolution. The four point density layers  
335 are made available in the data repository as auxiliary data together with the derived LiDAR metrics (see  
336 Sect. 7).





### 337 3.4 Limitations and usage notes

#### 338 3.4.1 Classification related errors and masks

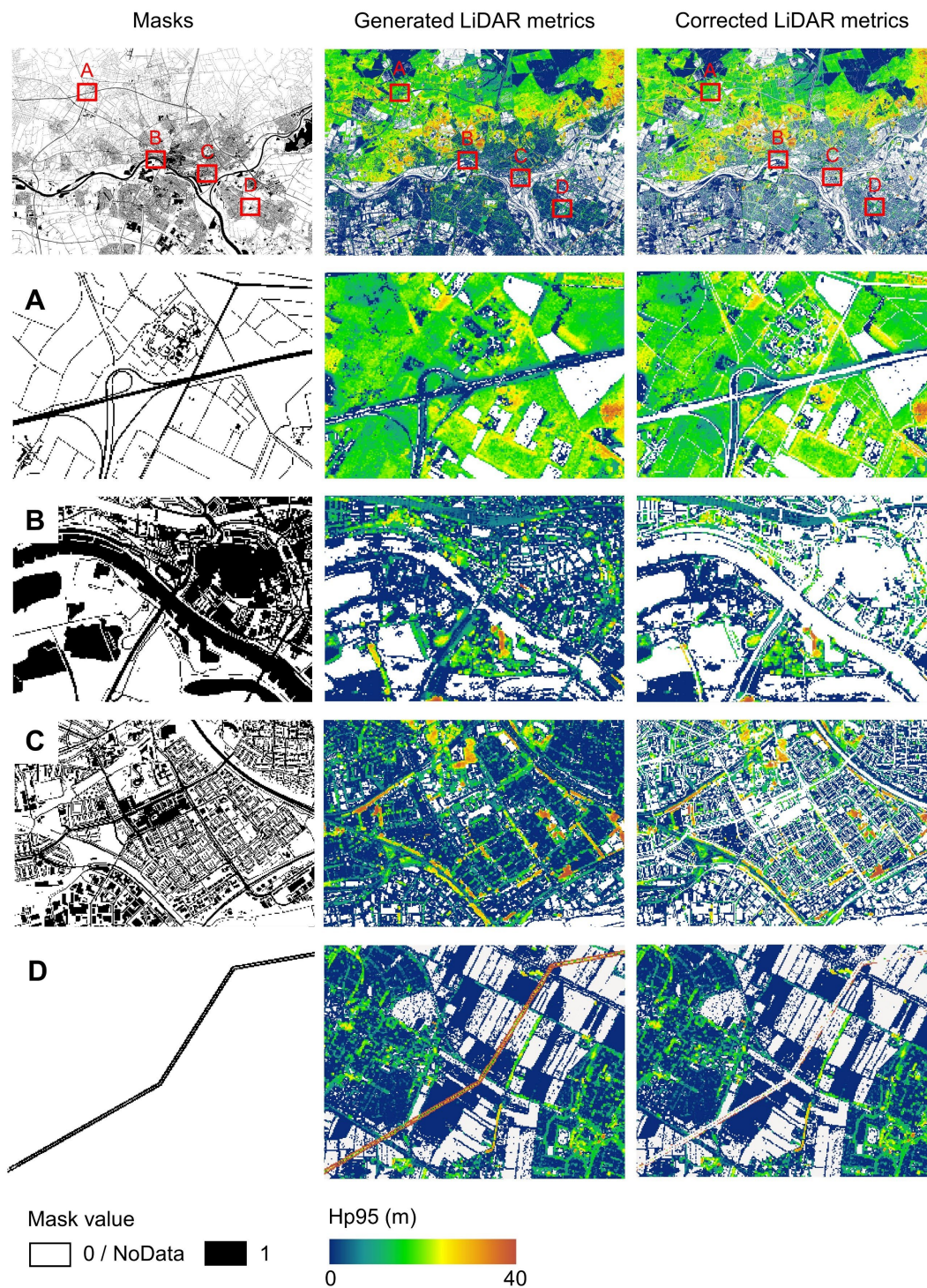
339 In the pre-classification of the raw AHN point clouds, there is no “vegetation” class provided based on  
340 the ASPRS standard (i.e. class 3: low vegetation, class 4: medium vegetation, or class 5: high vegetation).  
341 Instead, the vegetation points in the raw AHN1 and AHN2 datasets are included in the non-ground class  
342 (“uitgefilterd”, classification value of 0), whereas they belong to the class “unclassified” (classification  
343 value 1) in the AHN3 and AHN4 datasets (Table 1). This can introduce errors and biases when using the  
344 “uitgefilterd” or “unclassified” class for calculating ecosystem structure properties because points  
345 belonging to human infrastructures can still be included in these classes. Particularly, buildings and  
346 bridges are included (together with other objects other than ground) in the class “uitgefilterd” in the AHN1  
347 and AHN2 datasets, while they are classified separately (buildings in class 6: “buildings”, and bridges in  
348 class 26: “reserved”) in the AHN3 and AHN4 dataset — eliminating the errors caused by buildings and  
349 bridges in the final data products of the AHN3 and AHN4. Powerlines are not separated from the  
350 “uitgefilterd” class in the AHN1 and AHN2 datasets, and included in the class “unclassified” in the AHN3  
351 dataset, but they are classified separately in the AHN4 dataset as class 14: “powerline”. Yet, other human  
352 objects and infrastructures (e.g. cars, fences, and transmission towers) are not separated in any of the four  
353 AHN datasets and thus included in the non-ground class (“uitgefilterd”) of the AHN1 and AHN2 datasets  
354 and in the class “unclassified” in the AHN3 and AHN4 datasets, introducing some errors and biases in  
355 the final data products. There are also points appearing on water surfaces (e.g. reflected by boats and  
356 birds) which are included in the class “uitgefilterd” or “unclassified”, causing inaccuracies in the final  
357 products. In a previous study (Kissling et al., 2023), the accuracy of the 25 LiDAR metrics generated  
358 from the AHN3 dataset was assessed, particularly in relation to the error caused by using the class  
359 “unclassified” for calculating ecosystem structure properties. The results showed that the overall accuracy  
360 of the generated LiDAR metrics was high ( $0.90 \pm 0.04$ ,  $n = 25$  LiDAR metrics, tested in 100 randomly  
361 selected plots throughout the Netherlands, with  $10 \text{ m} \times 10 \text{ m}$  size per plot), ranging from 0.87–1. It is  
362 worth noting that the impact of those errors on the 25 LiDAR metrics varies, for instance, a stronger bias  
363 (i.e. the difference between the generated LiDAR metrics and the ground truth) can be observed in height  
364 metrics describing the top canopy layer (i.e. Hmax and Hp95) than in other height metrics or in metrics  
365 of vegetation cover in the low strata (i.e. BR\_below\_1 and BR\_below\_5) (Kissling et al., 2023).

366 To minimize the inaccuracies of the data products caused by human infrastructures and water  
367 surfaces, we provide mask layers of water areas, roads, and buildings for both the AHN3 and AHN4 data  
368 products based on the Dutch cadaster data (TOP10NL) from 2018 (corresponding to AHN3) and 2021  
369 (corresponding to AHN4) (<https://www.kadaster.nl/zakelijk/producten/geo-informatie/topnl>, last access  
370 19 October 2024). TOP10NL is part of the Basic Topography Registry (BRT) which provides the standard  
371 topographic base files for the whole Netherlands. Like the LiDAR metrics, the masks are calculated at 10



372 m resolution with the RD\_new / EPSG 28992 projection coordinate system and provided as raster layers  
373 in GeoTIFF format. In the masks, water surfaces, buildings and roads were merged into one class with a  
374 pixel value assigned to 1 and the rest with a pixel value of 0 (Fig. 5). Since the historical versions of  
375 TOP10NL data are not available for AHN1 (1996–2003) and AHN2 (2007–2012), we can only provide  
376 the masks for the AHN3 and AHN4 datasets (see Sect. 7 for data availability). However, despite the  
377 potential changes in buildings and roads over time, it is still possible to apply the generated masks to all  
378 four AHN data products, for instance, to minimize errors and to have comparable areas of interest.

379         Since powerlines are not classified separately for AHN1–AHN3 datasets and thus included in the  
380 calculation, it may cause abnormal values of vegetation structure, especially for vegetation height and  
381 vegetation cover above 20 m (Shi and Kissling, 2023). However, points belonging to powerlines are  
382 classified separately in AHN4 (Table 1), which provides a way to minimize errors caused by powerlines  
383 in the data products generated from AHN1–AHN3. We therefore extracted all powerline points from the  
384 AHN4 raw point cloud and generated a mask (at 10 m resolution) where pixels containing powerlines are  
385 assigned a value 1 and the rest as NoData (Fig. 5). Since the transmission towers are not classified  
386 separately in all four AHN datasets, the mask only covers the powerlines but not the transmission towers.  
387 Users can apply the powerline mask generated from AHN4 to the data products from AHN1–AHN3 and  
388 consequently improve the comparability of the LiDAR metrics across time. Note that the powerline  
389 infrastructure may also change over time, and the classification of powerlines from the AHN4 may not  
390 be fully representative for powerline distributions in earlier time periods.



391  
392  
393  
394

Fig. 5 Examples of masking roads, water surfaces, and buildings from the 2018 Dutch cadaster data (areas A, B, and C) and powerlines generated from the AHN4 (area D). Illustrated is the rasterized mask (first column), the generated vegetation height metric (i.e. Hp95) from AHN3 (second column), and the

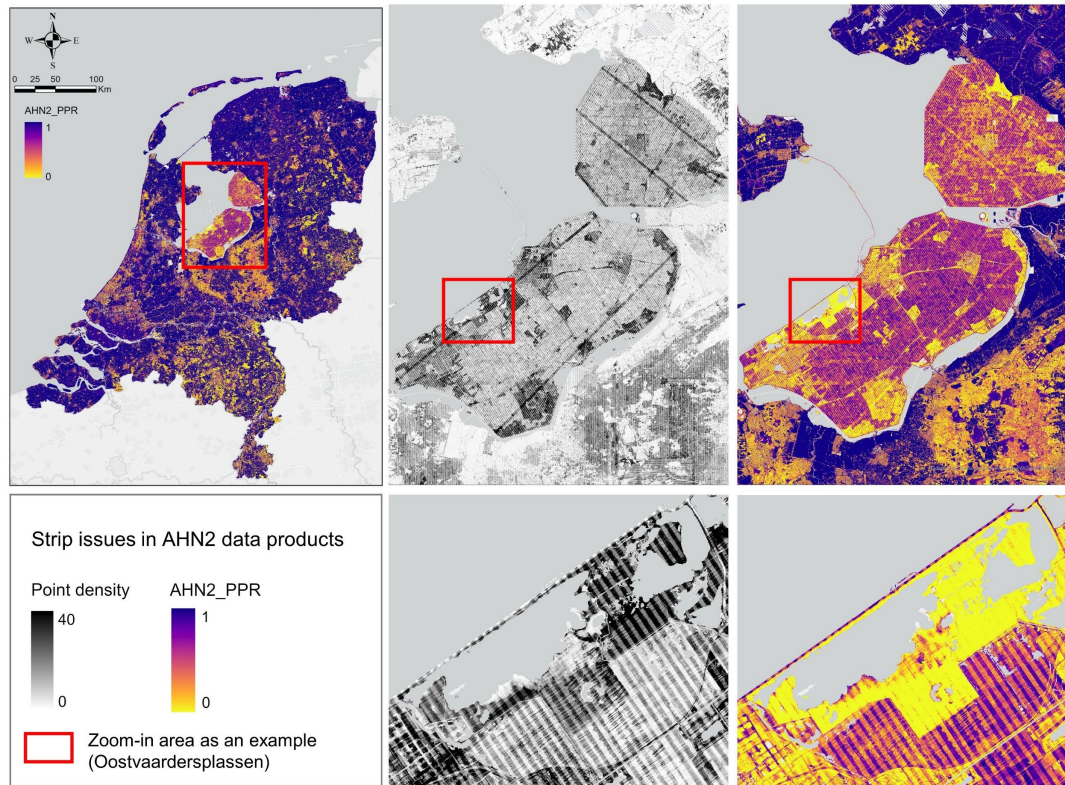




395 corrected LiDAR metric using the masks (third column). Four subareas show the inaccuracies in the  
396 originally generated LiDAR metric and the removal effect of using the mask for roads (area A), water  
397 (area B), buildings (area C), and powerlines (area D). A mask value of 1 represents the pixels with roads,  
398 water surfaces, buildings, and powerlines, while value 0 or NoData represents the rest. The masks and the  
399 LiDAR metrics are at  $10 \times 10$  m resolution.  $Hp95 = 95^{\text{th}}$  percentile of vegetation height.

### 400 3.4.2 Strip issues

401 Several strip patterns occur in the data products from AHN2 (Fig. 6). This strip issue specifically affects  
402 the pulse penetration ratio layer (representing vegetation openness), where both ground points (“ground”  
403 class) and vegetation points (“unclassified” class) were used for the metric calculation. A possible reason  
404 could be that the scan angle of the laser scanner used for point cloud acquisition was rather wide, and that  
405 the scanner thus has received more laser pulses from the areas located at the edges of the flight lines.  
406 Those overlapping areas (edges of the flight lines) often have a doubled point density, which also  
407 contributes to the strip patterns in the calculation of the LiDAR metrics using ground points (e.g. pulse  
408 penetration ratio). This issue only occurs in an area in the centre of the Netherlands (Fig. 6). Other LiDAR-  
409 derived vegetation metrics representing vegetation height, cover, and structural variability do not seem to  
410 be influenced by this strip issue. This strip issue was not observed in other AHN data products.



411  
412 Fig. 6 Strip issues in the AHN2 dataset. The point density (black and white, including all points) and the  
413 pulse penetration ratio (colour, representing vegetation openness) show similar strip patterns.



### 414 3.4.3 Abnormal values

415 A few pixels with abnormal values still exist in the final products. For instance, several pixels in the Hp95  
416 layer have a value higher than 100 m, which cannot represent the upper canopy of vegetation since the  
417 tallest tree in the Netherlands (a Douglas Fir, *Pseudotsuga menziesii*, i.e. a tall and fast-growing conifer  
418 native to western North America which was planted between 1860 and 1870 in Apeldoorn, the  
419 Netherlands) has been measured to be ~50 meter tall. More generally, most measurements of the tall trees  
420 in the Netherlands range between 20–45 m. Hence, abnormal values of vegetation height (e.g. > 50 m)  
421 most likely reflect the occurrence of human infrastructures that are not included in the AHN1 and AHN2  
422 class “uitgefilterd” or not sufficiently captured in the AHN3 and AHN4 classes “building” and “reserved”,  
423 e.g. aerial and radio masts (up to 350 m tall), tall industrial and meteorological towers and chimneys (50–  
424 200 m), cranes (50–130 m), elements of bridges (e.g. pylons and steel cables up to 140 m tall), wind  
425 turbines (up to 260 m) and powerlines (up to 80 m). Flying objects, such as birds and planes, can also be  
426 captured in the datasets, resulting in abnormal height values in the data products. We recommend filtering  
427 out those abnormal values before using the data products for further analysis, e.g. by removing grid cells  
428 with  $Hp95 > 50$  m.

429 Although the Netherlands has rather flat terrain, it is worth noting that the normalization method  
430 implemented in the Laserfarm workflow may introduce inaccuracies in normalized vegetation height  
431 values, especially if steep terrain occurs within a grid cell (Kissling et al., 2022). When applying the same  
432 workflow for other country or regions, abnormal values may occur in the areas with drastic topographic  
433 changes (e.g. cliffs, mountainous area). Users may consider using a different normalization method, for  
434 instance, normalizing non-ground points by subtracting the derived DTM from all points, or by  
435 interpolating the elevation of non-ground points using the exact position of ground points beneath  
436 (Roussel et al., 2020). Some studies also have suggested to use raw point clouds (e.g. the un-normalized  
437 DSM) to preserve the geometry of tree tops or plant area index profile in high slope areas (Khosravipour  
438 et al., 2015; Liu et al., 2017).

## 439 4 Demonstration of ecological use cases

### 440 4.1 Monitoring forest structural change across time using multi-temporal ALS data

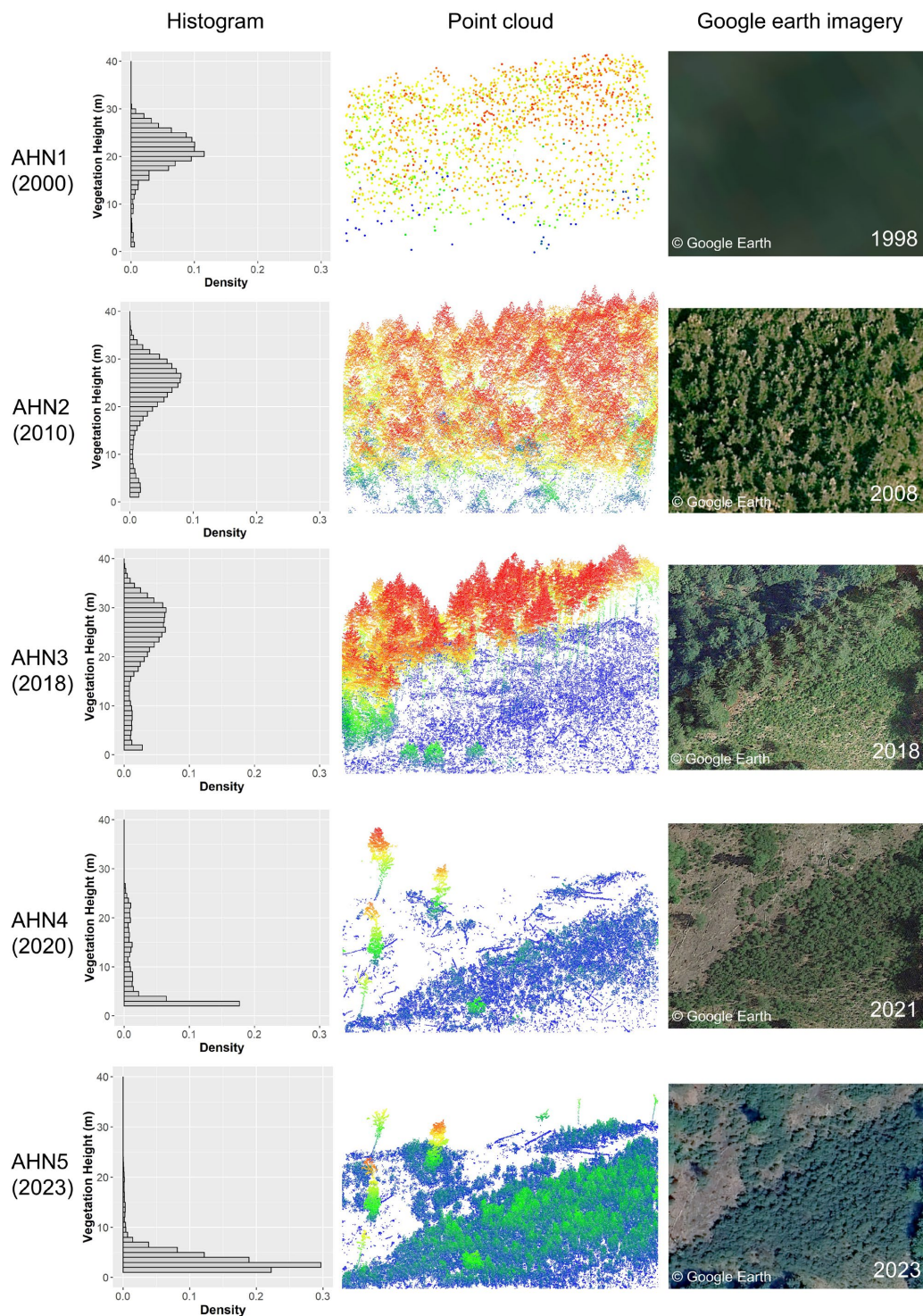
441 As a use case, we demonstrate here how the multi-temporal data products generated from the Dutch ALS  
442 surveys can capture forest structural change over the past two decades (2000–2023). We included the  
443 ongoing ALS campaign (AHN5) since the data were made available for the sample area (central location  
444 coordinates: 52.3250517°N, 5.7409230°E) at the time when the analysis was conducted. This provided a  
445 longer time series for detecting forest change. The sample area (in a forest area north of the national park  
446 De Hoge Veluwe) has experienced a clear forest cut in 2011 (between AHN2 and AHN3 surveys), with  
447 further forest loss and some regenerations captured by AHN4, while the latest AHN5 showed a forest



448 regrowth in the middle-low vegetation strata ( $< 10$  m) compared to AHN4 (Fig. 7). The histograms  
449 derived from point clouds from AHN1–AHN5 show the distribution of points shifting from tall vegetation  
450 (above 20 m, AHN1–AHN3) to low vegetation (below 10 m, AHN4 and AHN5). Due to the very low  
451 point density of the AHN1 data, detailed information on vegetation structure in the year 2000 is lacking.  
452 However, the histogram from AHN1 implies a similar pattern of canopy height as that from AHN2 (Fig.  
453 7). Google Earth imageries obtained on the closest dates available from each AHN survey also provide a  
454 good reference for the forest change events, except for the time of AHN1.

455 Six selected LiDAR-derived vegetation metrics derived from AHN1–AHN5 at 10 m resolution  
456 effectively capture the changes in vegetation structure over time (Fig. 8). The 95<sup>th</sup> percentile of vegetation  
457 height (Hp95) and mean vegetation height (Hmean) highlight reductions in forest canopy height due to  
458 cutting in 2011 (between AHN2 and AHN3) and in 2019 (between AHN3 and AHN4). The pulse  
459 penetration ratio (PPR) reveals shifts in vegetation openness, with openness peaking in AHN4, while the  
460 density of vegetation points at 2–3 m (BR\_2\_3) indicates regrowth in the understory, particularly in  
461 AHN4 and AHN5 (after 2021). The Shannon index (entropy\_z) reflects the vertical distribution of  
462 vegetation points (i.e. evenness), with AHN2 showing the highest value due to a more even point  
463 distribution of the canopy foliage before the canopy was cut. AHN3 shows the widest Shannon index  
464 range, capturing both high canopy trees and new re-growth. The standard deviation (i.e. vertical  
465 variability) of vegetation height (Hstd) shows a similar pattern as seen in Hp95.

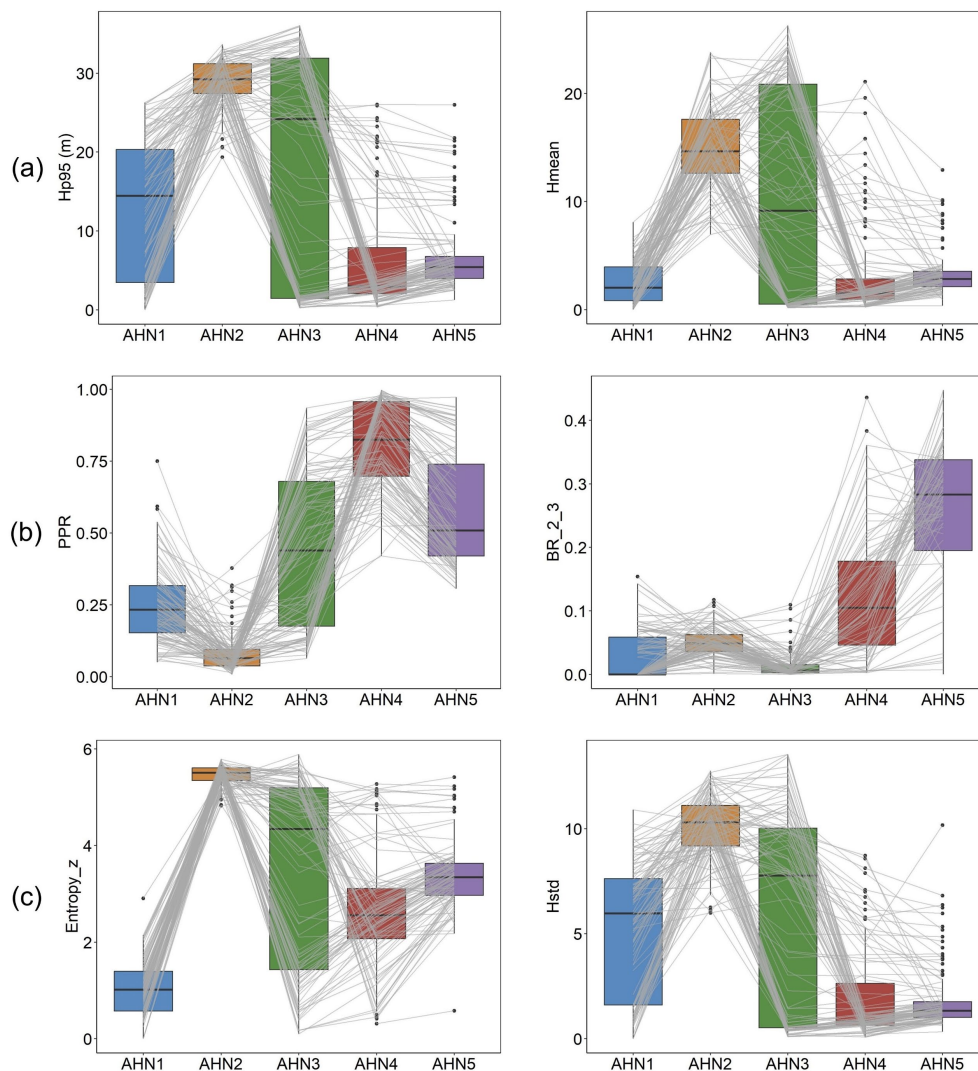




466  
467 Fig. 7 Forest structural change in a sample plot (100 m × 100 m) between 1998–2023 captured by the  
468 multi-temporal AHN datasets (AHN1–AHN5). The histograms were generated from each AHN point  
469 cloud, showing the distribution of the normalized vegetation height within the plot. The point clouds were



470 coloured by height (blue indicates lower vegetation height and red indicates higher vegetation height).  
471 AHN1 has a rather poor point density, but shows a histogram of vegetation height that is similar to AHN2.  
472 The forest cut can be observed from the point clouds of AHN3 and AHN4 compared to AHN2, with forest  
473 regrowth occurring in AHN5. Google Earth imageries from the example area show the changes of the  
474 forest. Note that the dates of the Google Earth imageries do not correspond exactly to the dates of the  
475 airborne laser scanning surveys, but to the closest dates available. Map data: © Google Earth.



476  
477 Fig. 8 Boxplots of LiDAR metrics derived from multi-temporal AHN datasets capturing the changes of  
478 the vegetation structure in a 100 m × 100 m sample area (compare Fig. 7). (a) The 95<sup>th</sup> percentile of  
479 vegetation height (Hp95) and the mean vegetation height (Hmean) representing vegetation height. (b) The  
480 pulse penetration ratio (PPR) and the density of vegetation points between 2–3 m (BR\_2\_3) representing  
481 vegetation cover. (c) The Shannon index (Entropy\_z) and the standard deviation of vegetation height  
482 (Hstd) representing vegetation structural variability. Boxes show the median and interquartile range, with





483 whiskers extending to 1.5 times the interquartile range and outliers are plotted as dots. Each grey line  
484 represents a single pixel (10 m × 10 m) value changing from AHN1–AHN5, showing the influence of the  
485 events on vegetation within each pixel (e.g. forest cut and regrowth).

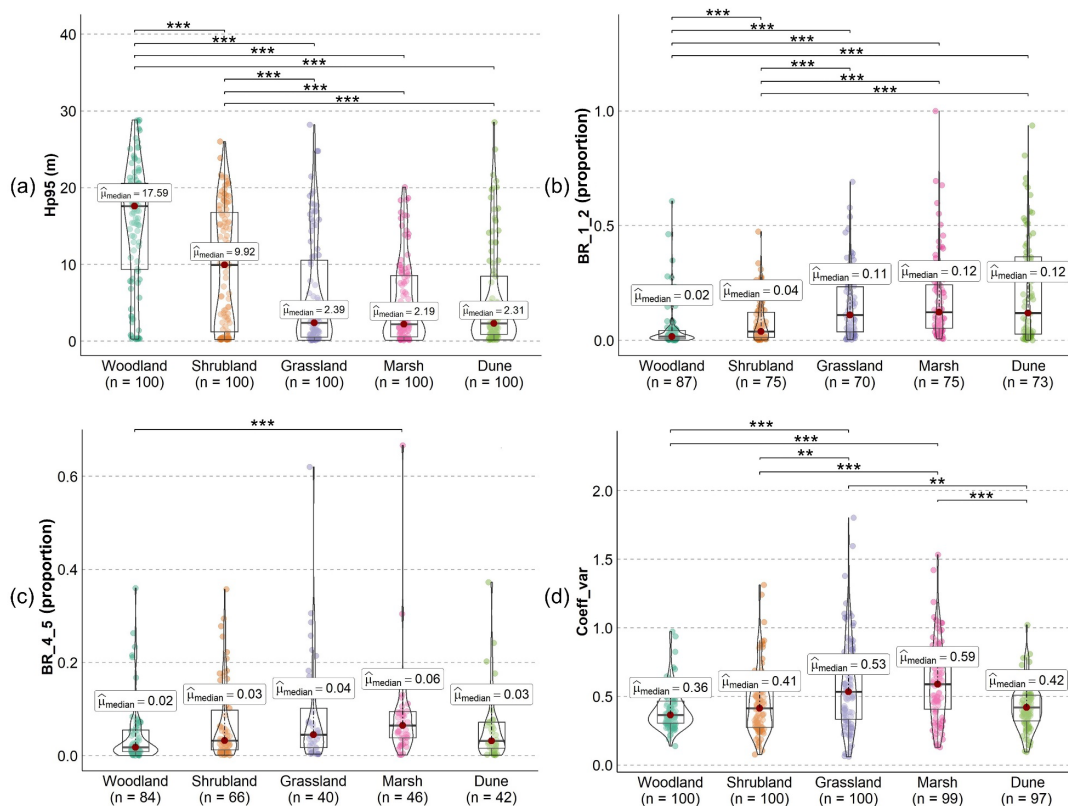
#### 486 **4.2 Comparison of vegetation structural difference within Natura 2000 sites**

487 In a second use case, we analyse how vegetation structure varies spatially across different Natura 2000  
488 habitat types in the Netherlands. Terrestrial habitats were categorized into five main classes: dunes,  
489 marshes, grasslands, shrublands, and woodlands, based on the dominant habitat type within each site (see  
490 details in Appendix A). For each habitat class, 100 random sample plots (10 m × 10 m, 500 plots in total)  
491 were selected where Hp95 is not NA (assuming vegetation occurring in the plots) (Figure A1). We used  
492 the data products from AHN4 for the analysis as they are the latest complete products for the whole  
493 Netherlands. Four LiDAR metrics were compared: the 95<sup>th</sup> percentile of vegetation height (Hp95),  
494 vegetation point density at 1–2 m (BR\_1\_2) and 4–5 m (BR\_4\_5), and the coefficient of variation in  
495 vegetation height (Coeff\_var). Structural differences among the five habitat types were assessed using the  
496 non-parametric Kruskal-Wallis test by ranks (Kruskal and Wallis, 1952), which compares two or more  
497 independent groups of equal or different sample sizes without assuming a normal distribution of the  
498 residuals. Pairwise comparisons of the statistical significance were conducted among groups (i.e. habitat  
499 types) using the Wilcoxon rank-sum test (Wilcoxon et al., 1970).

500 The strongest structural differences among the five habitat types were observed in canopy height  
501 (Hp95) and vegetation density in the lower strata (BR\_1\_2), followed by vegetation vertical variability  
502 (Coeff\_var) and vegetation density in the middle strata (BR\_4\_5) (Fig. 9). Canopy height (i.e. Hp95) of  
503 both woodlands and shrublands showed a statistically significant difference to all other habitat types,  
504 whereas grasslands, marshes and dunes did not differ in canopy height (Fig. 9a). The latter three habitat  
505 types showed a median canopy height of ~ 2.3 m, whereas it is around 9.9 m and 17.6 m for shrublands  
506 and woodlands, respectively. Vegetation density in the low vegetation stratum (between 1–2 m) also did  
507 not statistically differ between grasslands, marshes, and dunes (Fig. 9b). However, woodlands and  
508 shrublands with their more shaded understory and stronger light competition had much lower vegetation  
509 densities between 1–2 m than the three open habitat types (Fig. 9b). In the mid-layer (4–5 m), only the  
510 vegetation density of woodlands and marshes showed a statistically significant difference (Fig. 9c). The  
511 very low mid-layer density in woodlands may be due to the high canopy from trees limiting growth in the  
512 understory (e.g. shrubs), whereas shrubs and trees in marshes may generally have a lower canopy height  
513 than woodland trees, thus showing high vegetation density at 4–5 m. In terms of structural variability,  
514 grasslands and marshes have the highest median values of the coefficient of variation of vegetation height,  
515 showing significant differences to woodlands, shrublands and dunes (Fig. 9d). This probably reflects a  
516 high heterogeneity in vegetation structure in both grasslands and marshes, where a large variability from



517 low to high vegetation is captured within the 10 m × 10 m plots. It is also the only metric among the four  
 518 selected metrics where dunes showed statistically significant differences to grasslands and marshes.



519  
 520 Fig. 9 Comparison of ecosystem structure between five Natura 2000 habitat types using four different  
 521 LiDAR metrics of vegetation structure. (a) Canopy height (the 95<sup>th</sup> percentile of vegetation height, Hp95),  
 522 (b) vegetation density at 1–2 m (BR\_1\_2), (c) vegetation density at 4–5 m (BR\_4\_5), and (d) structural  
 523 variability of vegetation height (coefficient of variation in vegetation height, Coeff\_var). The bars above  
 524 the violin plot indicate whether there is a statistical significance between two compared habitat types. The  
 525 pairwise comparisons of the statistical significance were conducted using the Wilcoxon rank-sum test  
 526 after the non-parametric Kruskal-Wallis test by ranks. The significant level is marked as follows: \*\*\* ( $p$   
 527  $< 0.001$ ), \*\* ( $p < 0.01$ ), and \* ( $p < 0.05$ ). Red dots indicate the median value ( $\hat{\mu}_{median}$ ) of the LiDAR  
 528 metrics measured for each habitat type. Note that not all sampled plots have vegetation points (from class  
 529 “unclassified”) between 1–2 m and between 4–5 m, therefore the total number of sample plots for the  
 530 “BR\_1\_2” and “BR\_4\_5” analysis was  $< 100$  for each habitat type (after removing NA value). The NA  
 531 value also occurs for “Coeff\_var” when there is only one point (from class “unclassified”) in the sampled  
 532 plot (see metric calculation in Table 3).

## 533 5 Discussion

534 We present a set of multi-temporal high-resolution data products of ecosystem structure derived from  
 535 country-wide ALS surveys of the Netherlands (AHN1–AHN4), capturing vegetation structure dynamics  
 536 over the past two decades (1998–2022). For each AHN dataset, we provide 25 LiDAR-derived vegetation



537 metrics as GeoTIFF raster layers representing vegetation height, vegetation cover, and vegetation  
538 structural variability at 10 m resolution. In total, we processed ~ 70 TB (uncompressed) raw point clouds  
539 from four national ALS surveys into ~ 59 GB GeoTIFF raster layers as final data products. These data  
540 products hold great value for ecological and geospatial applications, including species distribution  
541 modelling, habitat characterization, and forest and biodiversity dynamics monitoring. The availability of  
542 these ready-to-use LiDAR metrics enables ecologists and researchers to integrate detailed ecosystem  
543 structural information from complex 3D point clouds into their studies without the burden of handling  
544 large ALS datasets and computational challenges. Additionally, the dataset serves as a valuable resource  
545 for detecting vegetation structural changes and analysing ecosystem dynamics using multi-temporal  
546 remote sensing techniques.

547         Several key aspects should be considered when utilizing the presented data products. First, many  
548 commonly used LiDAR-derived metrics, especially those related to vegetation height (e.g. maximum  
549 vegetation height, 95<sup>th</sup> percentile height, mean height), are often highly correlated (Kissling and Shi, 2023;  
550 Shi et al., 2018a). To gain a more comprehensive understanding of ecosystem structure, it is advisable to  
551 use a complementary set of LiDAR metrics that captures different dimensions of ecosystem structure, or  
552 to use dimensionality reduction methods (such as a principal component analysis) to avoid multi-  
553 collinearity (Kissling and Shi, 2023). For instance, using the coefficient of variation of vegetation height  
554 (Coeff\_var) instead of the standard deviation (Hstd) as a metric of structural variability can avoid  
555 correlations with mean or canopy vegetation height (Hmean and Hp95) (Kissling and Shi, 2023). Second,  
556 vegetation cover in different height layers is a crucial component of forests and other ecosystems,  
557 influencing energy fluxes between the ecosystem and the atmosphere (Shugart et al., 2010; Toivonen et  
558 al., 2023). Unlike the cover metrics proposed by Moudrý et al. (2022), where herbaceous, shrub and tree  
559 layers were used to represent different vegetation strata, our metrics use fixed height intervals (e.g. 1–2  
560 m, 2–3 m, 3–4 m, 4–5 m, 5–20 m, above 20 m) to ensure applicability across diverse ecosystems. Not all  
561 ecosystems share the same vegetation growth forms, making these height bin-defined metrics more  
562 ecosystem-agnostic. The cover metrics from different height layers can be used as predictors of animal  
563 species richness (Goetz et al., 2007), species distributions (Davies and Asner, 2014), and habitat  
564 characteristics (Vierling et al., 2008; Bakx et al., 2019). Third, LiDAR metrics related to vegetation  
565 structural variability (e.g. Hstd, Hskew, and Hkurt) are often influenced by various ecological and sensing  
566 methodology-related factors, making them potentially challenging to interpret (Assmann et al., 2022).  
567 However, metrics representing structural variability are valuable input for models assessing forest  
568 functional diversity and structural types, especially when combined with optical remote sensing  
569 (Kamoske et al., 2022; Zheng et al., 2021). Thus, careful selection of LiDAR metrics for specific  
570 applications is highly recommended. Terrain and surface descriptors such as DTMs and DSMs (or canopy  
571 height model as derivative) can be additionally considered because they are important for forest and  
572 habitat classifications (Shoot et al., 2021), quantifying soil moisture or wetness (Assmann et al., 2022),



573 and analysing species composition (Toivonen et al., 2023; Hill and Thomson, 2005). However, since the  
574 AHN programme has already provided DTM and DSM layers for the AHN2, AHN3, and AHN4 datasets  
575 at 0.5 m and 5 m resolutions in their repository, we did not reproduce these data products.

576 While multi-temporal ALS data offer valuable insights into fine-scale vegetation structural  
577 changes and ecosystem dynamics, there are also notable challenges, especially when performing change  
578 detection across point clouds with different characteristics, such as point density, scanning angle, and  
579 varying vertical and horizontal accuracy (White et al., 2016). Instead of performing change detection  
580 directly on point clouds (Xu et al., 2015; Kharroubi et al., 2022), many studies use rasterized LiDAR  
581 metrics for monitoring changes on vegetation structure. This is less computational intensive and better  
582 suited for areas with complex vegetation structure as it regularizes complex 3D point cloud information  
583 onto a 2D grid (Vastaranta et al., 2013; Choi et al., 2023). Several commonly used change detection  
584 methods can be applied to the multi-temporal data with rasterized LiDAR metrics. These include image  
585 differencing (i.e. subtracting the pixel values of one raster layer, such as Hp95 from AHN3, from the  
586 other, such as Hp95 from AHN4), threshold-based change detection (i.e. classifying the pixels as  
587 “changed” or “unchanged” based on a set threshold after image differencing), and post-classification  
588 comparison (i.e. comparing classified raster layers, such as maps of vegetation types based on derived  
589 LiDAR metrics, from different time periods) (Noordermeer et al., 2019; Dalponte et al., 2019). Those  
590 methods can be applied to the provided AHN data products, especially after masking water areas, roads,  
591 buildings, and powerlines. Change metrics derived from multi-temporal LiDAR data can also be  
592 combined with clustering methods to characterize areas of structural changes, such as modifications of  
593 forests by the eastern spruce budworm (Trotto et al., 2024). Together with the development of deep  
594 learning on change detection (Bai et al., 2023), more in-depth insights from the presented AHN datasets  
595 can be revealed, enabling accurate and comprehensive analysis of ecosystem dynamics. Given the  
596 consistent coordinate system used in the four AHN datasets (EPSG: 28992, NAP: 5709; see Table 1),  
597 additional georeferencing steps are unnecessary before conducting further analysis with the data products  
598 that we provide. The scan angle, overlapping rate, and vertical accuracy of AHN2–AHN4 are rather  
599 comparable (Table 1), potentially reducing errors related to systematic differences across time. However,  
600 the data products are generated from point clouds with different point density, which may introduce  
601 inconsistencies in capturing vegetation structure. Nevertheless, analyses of tree growth using multi-  
602 temporal LiDAR data with different point density in forests of Scotland implied that the accuracy does  
603 not decrease as long as the point density is exceeding 7 pts m<sup>-2</sup> (Zhao et al., 2018). Several studies also  
604 indicated that the spatial distribution of the point cloud remains similar even if the point density varies  
605 and increasing point density does not increase area-based estimation accuracy (Hudak et al., 2012; Fekety  
606 et al., 2015; Cao et al., 2016). We therefore anticipate that the data products from AHN2, AHN3, and  
607 AHN4 are sufficiently comparable for reliable change detection. However, due to the low point density



608 and reduced accuracy, we do not recommend including the data products from AHN1 in multi-temporal  
609 analyses.

610 All software and tools employed in the pipeline for producing the data products are free and open-  
611 source, ensuring a standardized yet flexible processing framework for country-wide ALS data and  
612 enabling reproducibility for future surveys. While existing ALS processing software such as OPALS  
613 (Pfeifer et al., 2014) and LAStools (<http://lastools.org/>) are not (fully) open-source, and others like  
614 FUSION (<https://forsys.sefs.uw.edu/fusion/fusionlatest.html>), CloudCompare  
615 (<https://www.danielgm.net/cc/>), and lidR (Roussel et al., 2020) lack horizontal scalability and do not  
616 provide reproducible end-to-end workflows for large ALS datasets, the employed “Laserfarm” workflow  
617 fills a niche by addressing these challenges. Laserfarm is a high-throughput, modular, and reproducible  
618 end-to-end workflow designed for efficiently extracting LiDAR metrics of ecosystem structure using  
619 distributed computing infrastructures (Kissling et al., 2022). With the workflow materials that we provide,  
620 users can implement additional pre-processing steps (e.g. splitting, reclassification) and customize  
621 required parameters based on the input ALS data and available computing resources. The demonstrated  
622 configurations of IT infrastructure, computational cost, and time efficiency for processing multi-temporal  
623 AHN datasets serve as a reference for users to estimate the processing requirements for future national or  
624 regional ALS datasets. It is worth noting that the normalization method implemented in the Laserfarm  
625 workflow subtracts the elevation of the lowest point within a given neighbourhood to remove the  
626 influence of the terrain. This approach was specifically chosen for its effectiveness in handling small  
627 ditches and canals that are common in the Dutch landscape, providing a straightforward way to generate  
628 positive height values after normalization. However, it may be less suited for capturing continuous  
629 normalized height values and fine-scale terrain variability in smaller grid cells (< 1 m) (Kissling et al.,  
630 2022).

631 The data products presented here also make a great contribution to multi-source data fusion in  
632 remote sensing and ecological research (Ghamisi et al., 2019). Through the two use cases in Sect. 4, we  
633 demonstrate the utility of these multi-temporal datasets for monitoring long-term forest dynamics and  
634 characterizing habitat types. These applications can be further extended to other studies, such as  
635 improving land cover classification accuracy, particularly for objects composed of similar materials (e.g.  
636 grasslands, shrubs, and trees). Moreover, the fusion of vegetation structural information from LiDAR,  
637 spectral data from optical remote sensing (e.g. high-resolution digital aerial photogrammetry, Landsat and  
638 Sentinel-2 imagery), climate data, and field measurements underscores the value of integrating  
639 complementary remote sensing data across diverse applications. These include wildlife habitat  
640 characterization (Boelman et al., 2016), tree species identification (Shi et al., 2018b), forest structure and  
641 carbon stock mapping (Li et al., 2024), as well as assessing disturbances and recovery of ecosystem  
642 process (Li et al., 2023). Additionally, combining ecosystem structure data from multiple LiDAR



643 platforms, such as terrestrial, drone-based, airborne, and spaceborne LiDAR, could provide a more  
644 comprehensive understanding of ecosystem structure, spanning from understory to canopy level and  
645 across local plots to national or continental level.

## 646 **6 Code availability**

647 Jupyter Notebooks for processing AHN datasets: <https://github.com/ShiYifang/AHN>  
648 Laserfarm workflow repository: <https://github.com/eEcoLiDAR/Laserfarm>  
649 Laserchicken software repository: <https://github.com/eEcoLiDAR/laserchicken>  
650 Code for downloading AHN dataset: [https://github.com/ShiYifang/AHN/tree/main/AHN\\_downloading](https://github.com/ShiYifang/AHN/tree/main/AHN_downloading)  
651 Code for generating masks for AHN datasets: [https://github.com/ShiYifang/AHN/tree/main/AHN\\_masks](https://github.com/ShiYifang/AHN/tree/main/AHN_masks)  
652 Code for demonstration of ecological use cases: [https://github.com/ShiYifang/AHN/tree/main/Use\\_case](https://github.com/ShiYifang/AHN/tree/main/Use_case)

## 653 **7 Data availability**

654 All data products from AHN1–AHN4 (25 GeoTIFF layers for each AHN dataset), three masks (two for  
655 roads, water surfaces, and buildings from both AHN3 and AHN4, and one for powerlines generated from  
656 AHN4), and four point density layers (for AHN1–AHN4) are available from a Zenodo repository  
657 (<https://doi.org/10.5281/zenodo.13940846>) (Shi and Kissling 2024). The data used for the demonstrated  
658 use cases are also provided in the same repository. A detailed description of the provided data can be  
659 found in the README file in the data repository.



## 660 **8 Conclusions**

661 Ecosystem structure information derived from country-wide ALS data becomes increasingly needed for  
662 biodiversity science and ecosystem monitoring. The multi-temporal data products of ecosystem structure  
663 and the employed workflow presented here not only provide ready-to-use information for ecosystem  
664 monitoring and modelling within the Netherlands, but also enable reproducing desired data products from  
665 existing and upcoming large-scale ALS data beyond the Netherlands. We highlight the capability of multi-  
666 temporal ALS data products in capturing ecosystem structural dynamics across time and their usability in  
667 combination with other data sources. We also carefully evaluated the limitations and usability of  
668 generated data products and provided solutions or recommendations for future processing and usage. We  
669 envisage that the provided data products and the employed workflow will empower a wider use and  
670 uptake of ecosystem structure information in biodiversity and ecosystem science, land management,  
671 natural resource conservation, and policy support and decision making.  
672





## 673 Appendix A

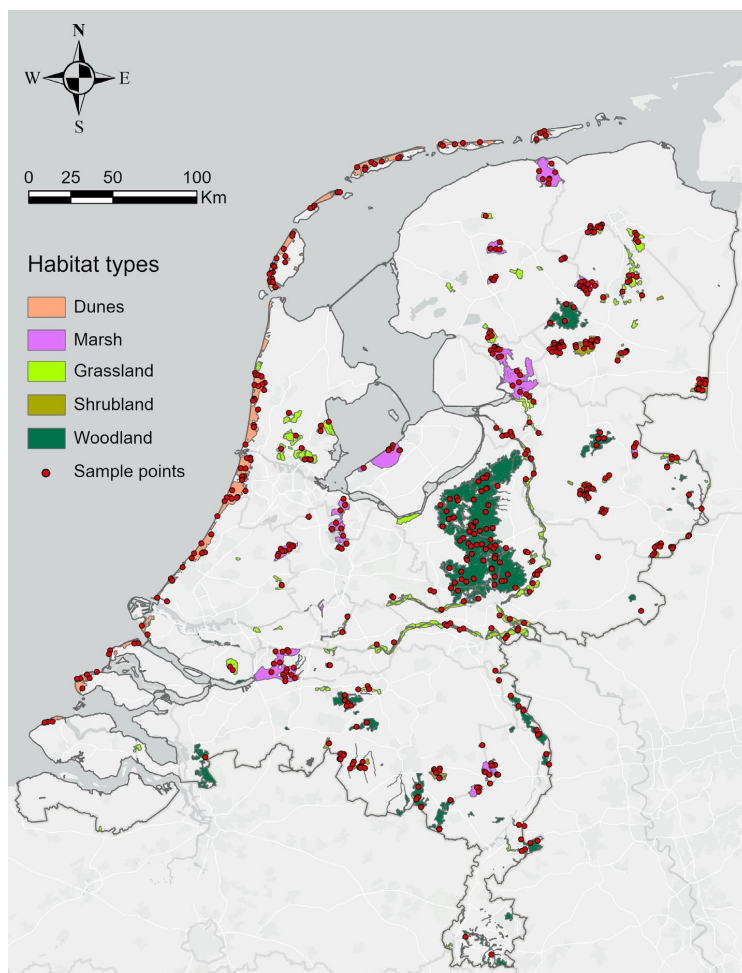
674 The source information about Natura 2000 sites was retrieved from the [Europe Environment Agency](#)  
675 (Natura 2000 (vector) - version 2021). The shapefile of the Natura 2000 sites and the attributes of each  
676 site that we used for the analysis were downloaded via  
677 <https://sdi.eea.europa.eu/datashare/s/JWt9KJCFMrPQDc7/download>. The information on the habitat  
678 class (from the table named “Natura2000\_end2021\_HABITATCLASS.csv”) was used to group them into  
679 five habitat types (i.e. dunes, marshes, shrublands, grasslands, and woodlands). The table contains the  
680 following information: description of the habitat class, habitat code, site code, and percentage of habitat  
681 composition within the site.

682 We first selected all the Natura 2000 sites within the Netherlands (i.e. SITECODE starting with  
683 NL), then summarized the highest percentage of habitat class within each site and grouped them into six  
684 main habitat types: water, dunes, marshes, shrubland, grassland, and woodland. For water, we included  
685 marine areas, sea inlets (habitat code: N01), tidal rivers, estuaries, mud flats, sand flats, and lagoons  
686 (habitat code: N02), and inland water bodies (habitat code: N06). For dunes, we included coastal sand  
687 dunes, sand beaches, and machair (habitat code: N04). For marsh, we included bogs, marshes, water  
688 fringed vegetation, and fens (habitat code: N07) and salt marshes, salt pastures, and salt steppes (habitat  
689 code: N03). For shrubland, we included heath, scrub, maquis and garrigue, and phygrana (habitat code:  
690 N08). For grassland, we included dry grassland, steppes (habitat code: N09), humid grassland, mesophile  
691 grassland (habitat code: N10), and improved grassland (habitat code: N14). For woodland, we included  
692 broadleaved deciduous woodland (habitat code: N16), coniferous woodland (habitat code: N17),  
693 evergreen woodland (habitat code: N18) and mixed woodland (habitat code: N19). For each Natura 2000  
694 site, the habitat type with the highest composition percentage was chosen as the dominate habitat. In total,  
695 there were 197 Natura 2000 sites within the Netherlands, including 36 water sites, 25 dune sites, 23 marsh  
696 sites, 17 shrubland sites, 54 grassland sites, and 42 woodland sites. For our study, we excluded water sites  
697 for the vegetation structure analysis (remaining 161 sites in total). For each habitat type, we randomly  
698 selected 100 sample plots (10 m × 10 m for each plot, i.e. in total 500 plots) where Hp95 is not NA  
699 (assuming vegetation occurring in the plots) using the *sampleRandom()* function in R (Figure A1). The  
700 shapefile of the 500 sample plots across the Natura 2000 sites was then used to extract the pixel values of  
701 the LiDAR metrics for comparison.

702 The shapefile of the Natura 2000 sites within the Netherlands (with habitat class information in attributes),  
703 100 sample plots for each habitat class, original and grouped habitat class information (.csv files), and the  
704 R processing script are provided in the data repository (see Sect. 7).

705





706

707 Figure A1. Natura 2000 sites and their habitat types in the Netherlands. The non-water habitat types were  
708 grouped into 5 classes (i.e. dunes, marshes, grasslands, shrublands, and woodlands) to conduct vegetation  
709 structure comparisons. For each class, we randomly sampled 100 plots (10 m × 10 m each) where Hp95  
710 was not NA (assuming that vegetation occurs in the plots) for the analysis ( $n = 500$  in total).

711



712 **Author contributions**

713 **Yifang Shi:** Conceptualization, Data curation, Formal analysis, Methodology, Validation, Visualization,  
714 Writing – original draft, Writing – review & editing. **W. Daniel Kissling:** Conceptualization,  
715 Investigation, Funding acquisition, Project administration, Supervision, Writing – review & editing.

716 **Competing interests**

717 The contact author has declared that none of the authors has any competing interests.

718 **Acknowledgements**

719 We acknowledge funding support from the European Commission (MAMBO project grant number  
720 101060639) and the Netherlands eScience Center (grant number ASDI.2016.014). We thank Francesco  
721 Nattino and Meiert W. Grootes from the Netherlands eScience Center for leading the development of the  
722 Laserfarm workflow through the project ‘eScience infrastructure for Ecological applications of LiDAR  
723 point clouds’ (eEcoLiDAR) (Kissling et al., 2017). The development of the data products was also  
724 supported by LifeWatch ERIC (<https://www.lifewatch.eu/>), a European research infrastructure  
725 consortium with focus on biodiversity and ecosystem research. We acknowledge the computing resources  
726 provided by SURF, the Dutch national facility for information and communication technology  
727 (<https://www.surf.nl/>).

728



## 729 References

- 730 Aguirre-Gutiérrez, J., WallisDeVries, M. F., Marshall, L., van't Zelfde, M., Villalobos-Arámbula, A. R.,  
731 Boekelo, B., Bartholomeus, H., Franzén, M., and Biesmeijer, J. C.: Butterflies show different functional  
732 and species diversity in relationship to vegetation structure and land use, *Global Ecology and*  
733 *Biogeography*, 26, 1126-1137, <https://doi.org/10.1111/geb.12622>, 2017.
- 734 ASPRS: LAS Specification 1.4-R15, 2019.
- 735 Assmann, J. J., Moeslund, J. E., Treier, U. A., and Normand, S.: EcoDes-DK15: high-resolution  
736 ecological descriptors of vegetation and terrain derived from Denmark's national airborne laser scanning  
737 data set, *Earth Syst. Sci. Data*, 14, 823-844, <https://10.5194/essd-14-823-2022>, 2022.
- 738 Bai, T., Wang, L., Yin, D., Sun, K., Chen, Y., Li, W., and Li, D.: Deep learning for change detection in  
739 remote sensing: a review, *Geo-spatial Information Science*, 26, 262-288,  
740 <https://doi.org/10.1080/10095020.2022.2085633>, 2023.
- 741 Bakx, T. R. M., Koma, Z., Seijmonsbergen, A. C., and Kissling, W. D.: Use and categorization of Light  
742 Detection and Ranging vegetation metrics in avian diversity and species distribution research, *Diversity*  
743 *and Distributions*, 25, 1045-1059, <https://doi.org/10.1111/ddi.12915>, 2019.
- 744 Boelman, N. T., Holbrook, J. D., Greaves, H. E., Krause, J. S., Chmura, H. E., Magney, T. S., Perez, J.  
745 H., Eitel, J. U. H., Gough, L., Vierling, K. T., Wingfield, J. C., and Vierling, L. A.: Airborne laser scanning  
746 and spectral remote sensing give a bird's eye perspective on arctic tundra breeding habitat at multiple  
747 spatial scales, *Remote Sensing of Environment*, 184, 337-349, <https://doi.org/10.1016/j.rse.2016.07.012>,  
748 2016.
- 749 Brand, G., Crombaghs, M., Oude Elberink, S., Brügelmann, R., and de Min, E.: Precisiebeschrijving  
750 AHN 2002, Rijkswaterstaat AGI, 2003.
- 751 Cao, L., Coops, N. C., Innes, J. L., Sheppard, S. R. J., Fu, L., Ruan, H., and She, G.: Estimation of forest  
752 biomass dynamics in subtropical forests using multi-temporal airborne LiDAR data, *Remote Sensing of*  
753 *Environment*, 178, 158-171, <https://doi.org/10.1016/j.rse.2016.03.012>, 2016.
- 754 Choi, D. H., LaRue, E. A., Atkins, J. W., Foster, J. R., Matthes, J. H., Fahey, R. T., Thapa, B., Fei, S.,  
755 and Hardiman, B. S.: Short-term effects of moderate severity disturbances on forest canopy structure,  
756 *Journal of Ecology*, 111, 1866-1881, <https://doi.org/10.1111/1365-2745.14145>, 2023.
- 757 Dalponte, M., Jucker, T., Liu, S., Frizzera, L., and Gianelle, D.: Characterizing forest carbon dynamics  
758 using multi-temporal lidar data, *Remote Sensing of Environment*, 224, 412-420,  
759 <https://doi.org/10.1016/j.rse.2019.02.018>, 2019.
- 760 Davies, A. B. and Asner, G. P.: Advances in animal ecology from 3D-LiDAR ecosystem mapping, *Trends*  
761 *in Ecology & Evolution*, 29, 681-691, <https://doi.org/10.1016/j.tree.2014.10.005>, 2014.
- 762 de Vries, J. P. R., Koma, Z., WallisDeVries, M. F., Kissling, W. D., and Tingley, R.: Identifying fine-  
763 scale habitat preferences of threatened butterflies using airborne laser scanning, *Diversity and*  
764 *Distributions*, 27, 1251-1264, <https://doi.org/10.1111/ddi.13272>, 2021.
- 765 Fekety, P. A., Falkowski, M. J., and Hudak, A. T.: Temporal transferability of LiDAR-based imputation  
766 of forest inventory attributes, *Canadian Journal of Forest Research*, 45, 422-435,  
767 <https://doi.org/10.1139/cjfr-2014-0405>, 2015.
- 768 Feng, T., Duncanson, L., Hancock, S., Montesano, P., Skakun, S., Wulder, M. A., White, J. C., Minor,  
769 D., and Loboda, T.: Characterizing Fire-Induced Forest Structure and Aboveground Biomass Changes in  
770 Boreal Forests Using Multitemporal Lidar and Landsat, *IEEE Journal of Selected Topics in Applied Earth*  
771 *Observations and Remote Sensing*, 17, 10108-10125, <https://doi.org/10.1109/JSTARS.2024.3400218>,  
772 2024.
- 773 Ghamisi, P., Rasti, B., Yokoya, N., Wang, Q., Hofle, B., Bruzzone, L., Bovolo, F., Chi, M., Anders, K.,  
774 and Gloaguen, R.: Multisource and multitemporal data fusion in remote sensing: A comprehensive review



- 775 of the state of the art, *IEEE Geoscience and Remote Sensing Magazine*, 7, 6-39,  
776 <https://doi.org/10.1109/MGRS.2018.2890023>, 2019.
- 777 Goetz, S., Steinberg, D., Dubayah, R., and Blair, B.: Laser remote sensing of canopy habitat heterogeneity  
778 as a predictor of bird species richness in an eastern temperate forest, USA, *Remote Sensing of*  
779 *Environment*, 108, 254-263, <https://doi.org/10.1016/j.rse.2006.11.016>, 2007.
- 780 Hein, L., Remme, R. P., Schenau, S., Bogaart, P. W., Lof, M. E., and Horlings, E.: Ecosystem accounting  
781 in the Netherlands, *Ecosystem Services*, 44, 101118, <https://doi.org/10.1016/j.ecoser.2020.101118>, 2020.
- 782 Hill, R. A. and Thomson, A. G.: Mapping woodland species composition and structure using airborne  
783 spectral and LiDAR data, *International Journal of Remote Sensing*, 26, 3763-3779,  
784 <https://doi.org/10.1080/01431160500114706>, 2005.
- 785 Hopkinson, C., Chasmer, L., and Hall, R. J.: The uncertainty in conifer plantation growth prediction from  
786 multi-temporal lidar datasets, *Remote Sensing of Environment*, 112, 1168-1180,  
787 <https://doi.org/10.1016/j.rse.2007.07.020>, 2008.
- 788 Hudak, A. T., Strand, E. K., Vierling, L. A., Byrne, J. C., Eitel, J. U. H., Martinuzzi, S., and Falkowski,  
789 M. J.: Quantifying aboveground forest carbon pools and fluxes from repeat LiDAR surveys, *Remote*  
790 *Sensing of Environment*, 123, 25-40, <https://doi.org/10.1016/j.rse.2012.02.023>, 2012.
- 791 Isenburg, M.: LAStools-Efficient LiDAR Processing Software (version 141017, academic), obtained  
792 from <http://rapidlasso.com>, 2017.
- 793 Jetz, W., McGeoch, M. A., Guralnick, R., Ferrier, S., Beck, J., Costello, M. J., Fernandez, M., Geller, G.  
794 N., Keil, P., Merow, C., Meyer, C., Muller-Karger, F. E., Pereira, H. M., Regan, E. C., Schmeller, D. S.,  
795 and Turak, E.: Essential biodiversity variables for mapping and monitoring species populations, *Nature*  
796 *Ecology & Evolution*, 3, 539-551, <https://doi.org/10.1038/s41559-019-0826-1>, 2019.
- 797 Kamoske, A. G., Dahlin, K. M., Read, Q. D., Record, S., Stark, S. C., Serbin, S. P., and Zarnetske, P. L.:  
798 Towards mapping biodiversity from above: Can fusing lidar and hyperspectral remote sensing predict  
799 taxonomic, functional, and phylogenetic tree diversity in temperate forests?, *Global Ecology and*  
800 *Biogeography*, 31, 1440-1460, <https://doi.org/10.1111/geb.13516>, 2022.
- 801 Kharroubi, A., Poux, F., Ballouch, Z., Hajji, R., and Billen, R.: Three Dimensional Change Detection  
802 Using Point Clouds: A Review, *Geomatics*, 2, 457-485, <https://doi.org/10.3390/geomatics2040025>, 2022.
- 803 Khosravipour, A., Skidmore, A. K., Wang, T., Isenburg, M., and Khoshelham, K.: Effect of slope on  
804 treetop detection using a LiDAR Canopy Height Model, *ISPRS Journal of Photogrammetry and Remote*  
805 *Sensing*, 104, 44-52, <https://doi.org/10.1016/j.isprsjprs.2015.02.013>, 2015.
- 806 Kissling, W. D. and Shi, Y.: Which metrics derived from airborne laser scanning are essential to measure  
807 the vertical profile of ecosystems?, *Diversity and Distributions*, 29, 1315-1320,  
808 <https://doi.org/10.1111/ddi.13760>, 2023.
- 809 Kissling, W. D., Seijmonsbergen, A. C., Foppen, R. P. B., and Bouten, W.: eEcoLiDAR, eScience  
810 infrastructure for ecological applications of LiDAR point clouds: reconstructing the 3D ecosystem  
811 structure for animals at regional to continental scales, *Research Ideas and Outcomes*, 3, e14939,  
812 <https://doi.org/10.3897/rio.3.e14939>, 2017.
- 813 Kissling, W. D., Shi, Y., Koma, Z., Meijer, C., Ku, O., Nattino, F., Seijmonsbergen, A. C., and Grootes,  
814 M. W.: Laserfarm – A high-throughput workflow for generating geospatial data products of ecosystem  
815 structure from airborne laser scanning point clouds, *Ecological Informatics*, 72, 101836,  
816 <https://doi.org/10.1016/j.ecoinf.2022.101836>, 2022.
- 817 Kissling, W. D., Shi, Y., Koma, Z., Meijer, C., Ku, O., Nattino, F., Seijmonsbergen, A. C., and Grootes,  
818 M. W.: Country-wide data of ecosystem structure from the third Dutch airborne laser scanning survey,  
819 *Data in Brief*, 46, 108798, <https://doi.org/10.1016/j.dib.2022.108798>, 2023.
- 820 Kissling, W. D., Walls, R., Bowser, A., Jones, M. O., Kattge, J., Agosti, D., Amengual, J., Basset, A., van  
821 Bodegom, P. M., Cornelissen, J. H. C., Denny, E. G., Deudero, S., Egloff, W., Elmendorf, S. C., Alonso



- 822 García, E., Jones, K. D., Jones, O. R., Lavorel, S., Lear, D., Navarro, L. M., Pawar, S., Pirzl, R., Rüger,  
823 N., Sal, S., Salguero-Gómez, R., Schigel, D., Schulz, K.-S., Skidmore, A., and Guralnick, R. P.: Towards  
824 global data products of Essential Biodiversity Variables on species traits, *Nature Ecology & Evolution*,  
825 2, 1531-1540, <https://doi.org/10.1038/s41559-018-0667-3>, 2018.
- 826 Koma, Z., Seijmonsbergen, A. C., and Kissling, W. D.: Classifying wetland-related land cover types and  
827 habitats using fine-scale lidar metrics derived from country-wide Airborne Laser Scanning, *Remote  
828 Sensing in Ecology and Conservation*, 7, 80-96, <https://doi.org/10.1002/rse2.170>, 2021a.
- 829 Koma, Z., Grootes, M. W., Meijer, C. W., Nattino, F., Seijmonsbergen, A. C., Sierdsema, H., Foppen, R.,  
830 and Kissling, W. D.: Niche separation of wetland birds revealed from airborne laser scanning, *Ecography*,  
831 44, 907-918, <https://doi.org/10.1111/ecog.05371>, 2021b.
- 832 Kruskal, W. H. and Wallis, W. A.: Use of ranks in one-criterion variance analysis, *Journal of the  
833 American statistical Association*, 47, 583-621, <https://www.jstor.org/stable/2280779>, 1952.
- 834 Kucharik, C. J., Foley, J. A., Delire, C., Fisher, V. A., Coe, M. T., Lenters, J. D., Young-Molling, C.,  
835 Ramankutty, N., Norman, J. M., and Gower, S. T.: Testing the performance of a dynamic global  
836 ecosystem model: water balance, carbon balance, and vegetation structure, *Global Biogeochemical  
837 Cycles*, 14, 795-825, <https://doi.org/10.1029/1999GB001138>, 2000.
- 838 Lamonaca, A., Corona, P., and Barbati, A.: Exploring forest structural complexity by multi-scale  
839 segmentation of VHR imagery, *Remote Sensing of Environment*, 112, 2839-2849,  
840 <https://doi.org/10.1016/j.rse.2008.01.017>, 2008.
- 841 Lefsky, M. A., Cohen, W. B., Parker, G. G., and Harding, D. J.: Lidar Remote Sensing for Ecosystem  
842 Studies: Lidar, an emerging remote sensing technology that directly measures the three-dimensional  
843 distribution of plant canopies, can accurately estimate vegetation structural attributes and should be of  
844 particular interest to forest, landscape, and global ecologists, *BioScience*, 52, 19-30,  
845 [https://doi.org/10.1641/0006-3568\(2002\)052\[0019:LRSFES\]2.0.CO;2](https://doi.org/10.1641/0006-3568(2002)052[0019:LRSFES]2.0.CO;2), 2002.
- 846 Li, H., Hiroshima, T., Li, X., Hayashi, M., and Kato, T.: High-resolution mapping of forest structure and  
847 carbon stock using multi-source remote sensing data in Japan, *Remote Sensing of Environment*, 312,  
848 114322, <https://doi.org/10.1016/j.rse.2024.114322>, 2024.
- 849 Li, Q., Bonebrake, T. C., Michalski, J. R., Kit Wong, F. K., and Fung, T.: Combining multi-temporal  
850 airborne LiDAR and Sentinel-2 multispectral data for assessment of disturbances and recovery of  
851 mangrove forests, *Estuarine, Coastal and Shelf Science*, 291, 108444,  
852 <https://doi.org/10.1016/j.ecss.2023.108444>, 2023.
- 853 Lin, Y.-C., Shao, J., Shin, S.-Y., Saka, Z., Joseph, M., Manish, R., Fei, S., and Habib, A.: Comparative  
854 Analysis of Multi-Platform, Multi-Resolution, Multi-Temporal LiDAR Data for Forest Inventory,  
855 *Remote Sensing*, 14, 649, <https://doi.org/10.3390/rs14030649>, 2022.
- 856 Lindenmayer, D. B., Margules, C. R., and Botkin, D. B.: Indicators of Biodiversity for Ecologically  
857 Sustainable Forest Management, *Conservation Biology*, 14, 941-950, <https://doi.org/10.1046/j.1523-1739.2000.98533.x>, 2000.
- 859 Liu, J., Skidmore, A. K., Heurich, M., and Wang, T.: Significant effect of topographic normalization of  
860 airborne LiDAR data on the retrieval of plant area index profile in mountainous forests, *ISPRS Journal  
861 of Photogrammetry and Remote Sensing*, 132, 77-87, <https://doi.org/10.1016/j.isprsjprs.2017.08.005>,  
862 2017.
- 863 McCarley, T. R., Kolden, C. A., Vaillant, N. M., Hudak, A. T., Smith, A. M. S., Wing, B. M., Kellogg,  
864 B. S., and Kreitler, J.: Multi-temporal LiDAR and Landsat quantification of fire-induced changes to forest  
865 structure, *Remote Sensing of Environment*, 191, 419-432, <https://doi.org/10.1016/j.rse.2016.12.022>,  
866 2017.
- 867 Meijer, C., Grootes, M. W., Koma, Z., Dzigan, Y., Gonçalves, R., Andela, B., van den Oord, G.,  
868 Rangelova, E., Renaud, N., and Kissling, W. D.: Laserchicken—A tool for distributed feature calculation





- 869 from massive LiDAR point cloud datasets, *SoftwareX*, 12, 100626,  
870 <https://doi.org/10.1016/j.softx.2020.100626>, 2020.
- 871 Miura, N. and Jones, S. D.: Characterizing forest ecological structure using pulse types and heights of  
872 airborne laser scanning, *Remote Sensing of Environment*, 114, 1069-1076,  
873 <https://doi.org/10.1016/j.rse.2009.12.017>, 2010.
- 874 Moeslund, J. E., Zlinszky, A., Ejrnæs, R., Brunbjerg, A. K., Bøcher, P. K., Svenning, J.-C., and Normand,  
875 S.: Light detection and ranging explains diversity of plants, fungi, lichens, and bryophytes across multiple  
876 habitats and large geographic extent, *Ecological Applications*, 29, e01907,  
877 <https://doi.org/10.1002/eap.1907>, 2019.
- 878 Morsdorf, F., Mårell, A., Koetz, B., Cassagne, N., Pimont, F., Rigolot, E., and Allgöwer, B.:  
879 Discrimination of vegetation strata in a multi-layered Mediterranean forest ecosystem using height and  
880 intensity information derived from airborne laser scanning, *Remote Sensing of Environment*, 114, 1403-  
881 1415, <https://doi.org/10.1016/j.rse.2010.01.023>, 2010.
- 882 Moudrý, V., Cord, A. F., Gábor, L., Laurin, G. V., Barták, V., Gdulová, K., Malavasi, M., Rocchini, D.,  
883 Stereńczak, K., Prošek, J., Klápště, P., and Wild, J.: Vegetation structure derived from airborne laser  
884 scanning to assess species distribution and habitat suitability: The way forward, *Diversity and  
885 Distributions*, 29, 39-50, <https://doi.org/10.1111/ddi.13644>, 2022.
- 886 Musthafa, M. and Singh, G.: Improving forest above-ground biomass retrieval using multi-sensor L-and  
887 C-Band SAR data and multi-temporal spaceborne LiDAR data, *Frontiers in Forests and Global Change*,  
888 5, 822704, <https://doi.org/10.3389/ffgc.2022.822704>, 2022.
- 889 Nilsson, M., Nordkvist, K., Jonzén, J., Lindgren, N., Axensten, P., Wallerman, J., Egberth, M., Larsson,  
890 S., Nilsson, L., Eriksson, J., and Olsson, H.: A nationwide forest attribute map of Sweden predicted using  
891 airborne laser scanning data and field data from the National Forest Inventory, *Remote Sensing of  
892 Environment*, 194, 447-454, <https://doi.org/10.1016/j.rse.2016.10.022>, 2017.
- 893 Noordermeer, L., Økseter, R., Ørka, H. O., Gobakken, T., Næsset, E., and Bollandsås, O. M.:  
894 Classifications of Forest Change by Using Bitemporal Airborne Laser Scanner Data, *Remote Sensing*,  
895 11, 2145, <https://doi.org/10.3390/rs11182145>, 2019.
- 896 Noss, R. F.: Indicators for Monitoring Biodiversity: A Hierarchical Approach, *Conservation Biology*, 4,  
897 355-364, <https://doi.org/10.1111/j.1523-1739.1990.tb00309.x>, 1990.
- 898 Pereira, H. M., Ferrier, S., Walters, M., Geller, G. N., Jongman, R. H. G., Scholes, R. J., Bruford, M. W.,  
899 Brummitt, N., Butchart, S. H. M., Cardoso, A. C., Coops, N. C., Dulloo, E., Faith, D. P., Freyhof, J.,  
900 Gregory, R. D., Heip, C., Höft, R., Hurtt, G., Jetz, W., Karp, D. S., McGeoch, M. A., Obura, D., Onoda,  
901 Y., Pettorelli, N., Reyers, B., Sayre, R., Scharlemann, J. P. W., Stuart, S. N., Turak, E., Walpole, M., and  
902 Wegmann, M.: Essential Biodiversity Variables, *Science*, 339, 277-278,  
903 <https://doi.org/10.1126/science.1229931>, 2013.
- 904 Pfeifer, N., Mandlbürger, G., Otepka, J., and Karel, W.: OPALS – A framework for Airborne Laser  
905 Scanning data analysis, *Computers, Environment and Urban Systems*, 45, 125-136,  
906 <https://doi.org/10.1016/j.compenvurbsys.2013.11.002>, 2014.
- 907 Riofrío, J., White, J. C., Tompalski, P., Coops, N. C., and Wulder, M. A.: Harmonizing multi-temporal  
908 airborne laser scanning point clouds to derive periodic annual height increments in temperate mixedwood  
909 forests, *Canadian Journal of Forest Research*, 52, 1334-1352, <https://doi.org/10.1139/cjfr-2022-0055>,  
910 2022.
- 911 Roussel, J.-R., Auty, D., Coops, N. C., Tompalski, P., Goodbody, T. R. H., Meador, A. S., Bourdon, J.-  
912 F., de Boissieu, F., and Achim, A.: lidR: An R package for analysis of Airborne Laser Scanning (ALS)  
913 data, *Remote Sensing of Environment*, 251, 112061, <https://doi.org/10.1016/j.rse.2020.112061>, 2020.
- 914 Ruiz-Jaén, M. C. and Aide, T. M.: Vegetation structure, species diversity, and ecosystem processes as  
915 measures of restoration success, *Forest Ecology and Management*, 218, 159-173,  
916 <https://doi.org/10.1016/j.foreco.2005.07.008>, 2005.



- 917 Shi, Y., & Kissling, W. D.: Multi-temporal high-resolution data products of ecosystem structure derived  
918 from country-wide airborne laser scanning surveys of the Netherlands [Data set].  
919 Zenodo. <https://doi.org/10.5281/zenodo.13940846>, 2024
- 920 Shi, Y. and Kissling, W. D.: Performance, effectiveness and computational efficiency of powerline  
921 extraction methods for quantifying ecosystem structure from light detection and ranging, *GIScience &*  
922 *Remote Sensing*, 60, 2260637, <https://doi.org/10.1080/15481603.2023.2260637>, 2023.
- 923 Shi, Y., Wang, T., Skidmore, A. K., and Heurich, M.: Important LiDAR metrics for discriminating forest  
924 tree species in Central Europe, *ISPRS Journal of Photogrammetry and Remote Sensing*, 137, 163-174,  
925 <https://doi.org/10.1016/j.isprsjprs.2018.02.002>, 2018a.
- 926 Shi, Y., Skidmore, A. K., Wang, T., Holzwarth, S., Heiden, U., Pinnel, N., Zhu, X., and Heurich, M.:  
927 Tree species classification using plant functional traits from LiDAR and hyperspectral data, *International*  
928 *Journal of Applied Earth Observation and Geoinformation*, 73, 207-219,  
929 <https://doi.org/10.1016/j.jag.2018.06.018>, 2018b.
- 930 Shoot, C., Andersen, H.-E., Moskal, L. M., Babcock, C., Cook, B. D., and Morton, D. C.: Classifying  
931 Forest Type in the National Forest Inventory Context with Airborne Hyperspectral and Lidar Data,  
932 *Remote Sensing*, 13, 1863, <https://doi.org/10.3390/rs13101863>, 2021.
- 933 Shugart, H. H., Saatchi, S., and Hall, F. G.: Importance of structure and its measurement in quantifying  
934 function of forest ecosystems, *Journal of Geophysical Research: Biogeosciences*, 115,  
935 <https://doi.org/10.1029/2009JG000993>, 2010.
- 936 Swart, L.: How the Up-to-date Height Model of the Netherlands (AHN) became a massive point data  
937 cloud, *NCG KNAW*, 17, 17-32, 2010.
- 938 Toivonen, J., Kangas, A., Maltamo, M., Kukkonen, M., and Packalen, P.: Assessing biodiversity using  
939 forest structure indicators based on airborne laser scanning data, *Forest Ecology and Management*, 546,  
940 121376, <https://doi.org/10.1016/j.foreco.2023.121376>, 2023.
- 941 Tompalski, P., Coops, N. C., White, J. C., Goodbody, T. R. H., Hennigar, C. R., Wulder, M. A., Socha,  
942 J., and Woods, M. E.: Estimating Changes in Forest Attributes and Enhancing Growth Projections: a  
943 Review of Existing Approaches and Future Directions Using Airborne 3D Point Cloud Data, *Current*  
944 *Forestry Reports*, 7, 1-24, <https://doi.org/10.1007/s40725-021-00135-w>, 2021.
- 945 Trotto, T., Coops, N. C., Achim, A., Gergel, S. E., and Roeser, D.: Characterizing forest structural changes  
946 in response to non-stand replacing disturbances using bitemporal airborne laser scanning data, *Science of*  
947 *Remote Sensing*, 10, 100160, <https://doi.org/10.1016/j.srs.2024.100160>, 2024.
- 948 Valbuena, R., O'Connor, B., Zellweger, F., Simonson, W., Vihervaara, P., Maltamo, M., Silva, C. A.,  
949 Almeida, D. R. A., Danks, F., Morsdorf, F., Chirici, G., Lucas, R., Coomes, D. A., and Coops, N. C.:  
950 Standardizing ecosystem morphological traits from 3D information sources, *Trends in Ecology &*  
951 *Evolution*, 35, 656-667, <https://doi.org/10.1016/j.tree.2020.03.006>, 2020.
- 952 Vastaranta, M., Wulder, M. A., White, J. C., Pekkarinen, A., Tuominen, S., Ginzler, C., Kankare, V.,  
953 Holopainen, M., Hyyppä, J., and Hyyppä, H.: Airborne laser scanning and digital stereo imagery measures  
954 of forest structure: comparative results and implications to forest mapping and inventory update, *Canadian*  
955 *Journal of Remote Sensing*, 39, 382-395, <https://doi.org/10.5589/m13-046>, 2013.
- 956 Vepakomma, U., St-Onge, B., and Kneeshaw, D.: Response of a boreal forest to canopy opening:  
957 assessing vertical and lateral tree growth with multi-temporal lidar data, *Ecological Applications*, 21, 99-  
958 121, <https://doi.org/10.1890/09-0896.1>, 2011.
- 959 Vierling, K. T., Vierling, L. A., Gould, W. A., Martinuzzi, S., and Clawges, R. M.: Lidar: shedding new  
960 light on habitat characterization and modeling, *Frontiers in Ecology and the Environment*, 6, 90-98,  
961 <https://doi.org/10.1890/070001>, 2008.
- 962 White, J. C., Coops, N. C., Wulder, M. A., Vastaranta, M., Hilker, T., and Tompalski, P.: Remote Sensing  
963 Technologies for Enhancing Forest Inventories: A Review, *Canadian Journal of Remote Sensing*, 42,  
964 619-641, <https://doi.org/10.1080/07038992.2016.1207484>, 2016.



- 965 Wilcoxon, F., Katti, S., and Wilcox, R. A.: Critical values and probability levels for the Wilcoxon rank  
966 sum test and the Wilcoxon signed rank test, *Selected tables in mathematical statistics*, 1, 171-259, 1970.
- 967 Wolter, P. T., Townsend, P. A., and Sturtevant, B. R.: Estimation of forest structural parameters using 5  
968 and 10 meter SPOT-5 satellite data, *Remote Sensing of Environment*, 113, 2019-2036,  
969 <https://doi.org/10.1016/j.rse.2009.05.009>, 2009.
- 970 Xu, H., Cheng, L., Li, M., Chen, Y., and Zhong, L.: Using Octrees to Detect Changes to Buildings and  
971 Trees in the Urban Environment from Airborne LiDAR Data, *Remote Sensing*, 7, 9682-9704,  
972 <https://doi.org/10.3390/rs70809682>, 2015.
- 973 Zellweger, F., Braunisch, V., Baltensweiler, A., and Bollmann, K.: Remotely sensed forest structural  
974 complexity predicts multi species occurrence at the landscape scale, *Forest Ecology and Management*,  
975 307, 303-312, <https://doi.org/10.1016/j.foreco.2013.07.023>, 2013.
- 976 Zellweger, F., Roth, T., Bugmann, H., and Bollmann, K.: Beta diversity of plants, birds and butterflies is  
977 closely associated with climate and habitat structure, *Global Ecology and Biogeography*, 26, 898-906,  
978 <https://doi.org/10.1111/geb.12598>, 2017.
- 979 Zenner, E. K. and Hibbs, D. E.: A new method for modeling the heterogeneity of forest structure, *Forest  
980 Ecology and Management*, 129, 75-87, [https://doi.org/10.1016/S0378-1127\(99\)00140-1](https://doi.org/10.1016/S0378-1127(99)00140-1), 2000.
- 981 Zhao, K., Suarez, J. C., Garcia, M., Hu, T., Wang, C., and Londo, A.: Utility of multitemporal lidar for  
982 forest and carbon monitoring: Tree growth, biomass dynamics, and carbon flux, *Remote Sensing of  
983 Environment*, 204, 883-897, <https://doi.org/10.1016/j.rse.2017.09.007>, 2018.
- 984 Zheng, Z., Zeng, Y., Schneider, F. D., Zhao, Y., Zhao, D., Schmid, B., Schaepman, M. E., and Morsdorf,  
985 F.: Mapping functional diversity using individual tree-based morphological and physiological traits in a  
986 subtropical forest, *Remote Sensing of Environment*, 252, 112170,  
987 <https://doi.org/10.1016/j.rse.2020.112170>, 2021.
- 988